Using a Vertical array Receiver Function Method to Image the Subsurface of the Groningen Gas Field

UTRECHT UNIVERSITY

Maurits Daniël Beudeker 3826686
mauritsbeu@gmail.com

Supervised by:

Hanneke Paulssen
h.paulssen@uu.nl
Ivan Pires de Vasconcelos
i.vasconcelos@uu.nl
Wen Zhou
w.zhou@uu.nl

February 20, 2020

Universiteit Utrecht

Contents

Abstract

In this study, we determine the delay time of P-to-S conversions from earthquake sources using a vertical array-based receiver function method. This method was used to detect discontinuities below the Groningen gas field.

The signal that comes directly after the direct P-wave arrival, known as the P-wave coda, contains valuable information about the arrivals of additional waves. One of the waves that arrive in this coda is the PS-wave. The PS-wave is an S-wave with a P-wave origin; it has been converted at a strong contrast in velocity and/or density between two media. This contrast is called a discontinuity. Since S-waves travel slower than P-waves, we can measure the difference in P- and PS-wave arrival time to infer the depth at which this conversion took place.

Waves that arrive after the direct P-wave are usually obscured by the source time function of an earthquake. The source time function reflects the slip process at the source and depends on the magnitude and slip mechanism. The source time function overprints the coda wave arrivals due to its duration, and thus delayed phase arrivals cannot be directly identified from the seismogram. By doing a deconvolution of the P-wave coda of the horizontal component with the vertical component, we can remove the source time function and obtain a receiver function that reflects the P-to-S converted waves. This receiver function shows the delay times between the P-wave and subsequent PS-conversions.

In traditional receiver function studies, data from a single geophone at the surface are used to determine the depth of global scale discontinuities. In this study we use an array based method to determine the delay time between direct P-waves and their PS-conversions to infer small scale discontinuities. Using data from 3-component geophones placed in the abandoned borehole SDM-01 near Groningen, we have determined the depth of multiple discontinuities below the Groningen gas field.

---

1 Introduction

1.1 Problem Statement and Research Aim

A large portion of the Dutch subsurface has been mapped up to a depth of 3 kilometers. This structure has mainly been inferred from borehole analyses and by conducting reflection surveys. These methods are elaborate and costly. Therefore, old seismic sections are currently being reinterpreted in order to further constrain the deep structure of the Dutch subsurface. If we want to study the Dutch subsurface more accurately, a more efficient and economically viable method would be favorable.

We research the feasibility of a vertical array receiver function method. This method will be used to detect the delay time of PS-conversions originating at discontinuities below the Groningen gas field. Discontinuities, or interfaces, are defined as strong contrasts in velocity and/or impedance at depth. These contrasts are usually caused by a change in composition. By deconvolving the radial and vertical P-wave coda recorded on a 3-component geophone in a borehole, we will be able to obtain a receiver function from an earthquake. These receiver functions show the delay time between the direct P-wave and its converted PS-wave. The PS-delay time can subsequently be used to determine the depth where conversion took place. If this method proves useful, it can be used to map the deep subsurface as a complementary method alongside seismic research. We apply the vertical array receiver function method to process data from different earthquakes recorded at an array of geophones over a three month timespan. This means that we can apply the receiver function method on data that is passively gathered: instead of recording vibrations from artificial sources like in seismics, the geophone array records data from naturally occurring earthquake sources. The receiver function method does not require elaborate processing, and determining the delay time of PS-wave arrivals is a fairly trivial process. Thus if it proves useful it can be a valuable asset in subsurface exploration.

Knowledge of the deep subsurface can be used to interpret potential faults, and therefore to determine regions of possible seismic risk. Thus, developing a method that is quick and economical can be a useful tool in the field of earthquake risk management. Information of the deep subsurface is also valuable for the purpose of deep geothermal well drilling.

By applying a deconvolution method on geophone

data from ten geophones recorded in the abandoned borehole SDM-01 in the Groningen area, we obtain receiver functions from different earthquakes. The receiver functions from these earthquakes will then be compared to receiver functions obtained from an elastic one dimensional model. This model can help us determine the depth at which P-to-S conversion occurs.

1.2 Previous Research

The receiver function method has been described as early as 1979. In this research by Langston (1979), receiver functions have been obtained from teleseismic earthquakes to infer the structure below Mount Rainier, Washington. Teleseismic earthquakes are earthquakes at large distances from the receiver; the closest source used in that paper occured at an epicentral distance of 1,776 km, and the furthest event occured at nearly 10,000 km away from the geophone. By using events that were recorded on only one 3-component seismometer, Langston succeeded in showing arrivals of PS-conversions. After determining delay times of PS-conversions in events for different directions, it was concluded that PS-waves originated at an interface that ranged from 15 km to 20 km in depth. The interface causing these conversions was identified as the Mohorovičić discontinuity. It was also inferred that the discontinuity increased in depth in the North-northeastern direction.

The receiver function method has proven successful in other studies, eg; Owens et al. (1984), Ligorria and Ammon (1999) and Julia et al. (2000), were all successful in mapping the subsurface.

More recently, deployment of broadband seismic instruments has provided new applications for the receiver function method (Rondenay, 2009). An array based method was used to model the upper mantle (Xu et al. (2007), showing PS-conversions at a small scale.

A similar array based receiver function method has been used in Nábělek et al. (2009), where underplating in the Himalayan Mountain Range and the Tibetan Plateau was studied and the Himalayan crust below Nepal was successfully imaged.

Arwert (2019) used the receiver function method with a vertical array of geophones in order to verify the velocity profile in the abandoned borehole SDM-01. It was discovered that when using a vertical array of geophones, receiver functions can also be used to find PS-conversions on a small scale. Signals that might be attributed to noise have been identified as being P-to-S conversions. Because of the vertical alignment of the geophones in the borehole, the up-and downgoing phase arrivals can be seen travelling through the geophones. The receiver function method was used on downgoing waves coming from check shots in order to validate the existing velocity profile.

This investigation will build on the methods from these aforementioned studies to study upgoing waves coming from earthquakes recorded in borehole SDM-01. We show that a vertical geophone array can be used to detect upgoing PS-conversions, which have been used to infer the depth of discontinuities.

1.3 The Groningen Gas Field

The geophone array was placed in the abandoned borehole SDM-01 in the Groningen area (see figure 1.1), which was originally drilled for the purpose of the extraction of natural gas.

With a volume 2.8 Trillion cubic meters of gas and a subsurface area of 900 km^2, the Groningen gas field is the largest in Europe, and ever since its discovery in 1959, the gas field was a steady source of natural gas (Whaley, 2009).

While gas extraction has been very favorable for the Dutch economy, removing natural gas from the subsurface has its downsides: reduced pore pressure due to gas extraction has caused a stress change in the reservoir. This has led to induced seismicity, which in turn has led to damage to domestic property and other structures at the surface. This damage caused dissatisfaction among people living near the gas field.

Following a multitude of public complaints, the government has decided to cease gas extraction in the Groningen gas field as soon as 2022 (Geels, 2019).

In order to monitor this seismicity and prevent further damage, the Nederlandse Aardolie Maatschappij (NAM) has placed arrays of geophones in boreholes. These 3-component geophones measure displacement in three directions. Since these geophone arrays are placed at depth they are less sensitive to surface waves, noise occurring due to human activity, and microseismic occurrences. This grants the opportunity to study earthquake waves in more detail.

1.4 Geological Setting

Before studying the subsurface of the Groningen gas field we describe the local geology in this section:

The oldest detected formation in the Netherlands is from the Devonian age (359 - 416 Ma), which consists of a thick sandstone layer (Geluk et al., 2007). In the Southernmost part of the Netherlands, in the Brabant Massif, sandstone sediments were deposited from the middle Devonian until the late Devonian. This formation is imaged as a half-graben with normal faulting, which developed after extension in the Devonian. Devonian sandstones are not expected to extend towards

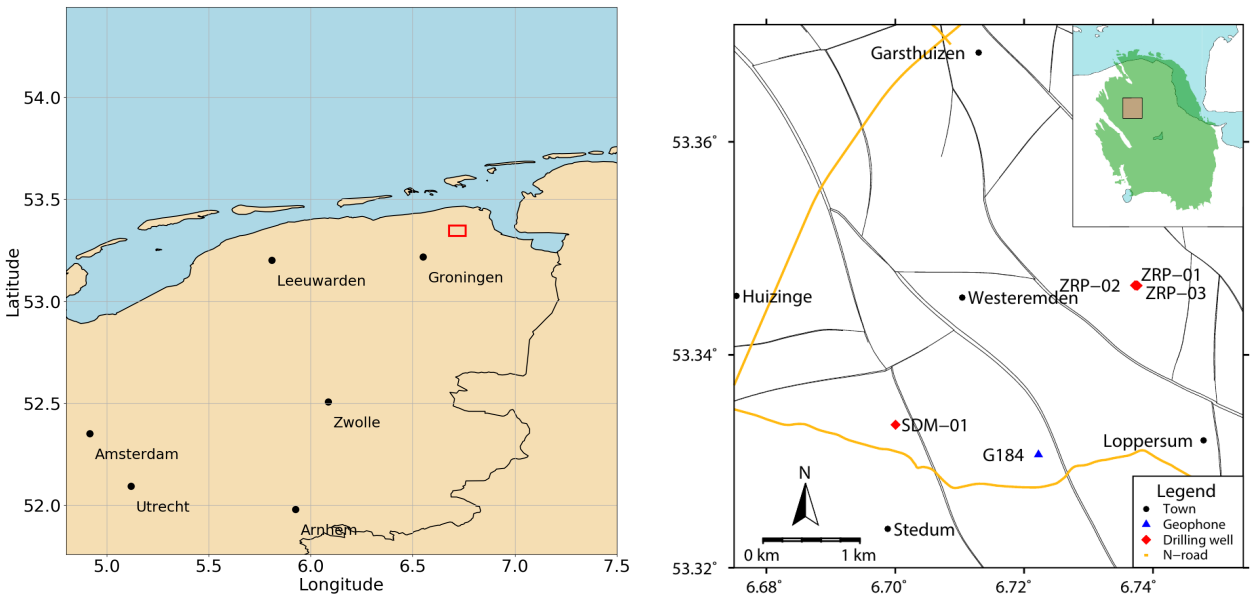

Figure 1.1: (left) The study region on a map of the Northeastern Netherlands. The study area is located in the red rectangle.
(right) Enlargement of the study area, from van Weers (2019). Here the location of borehole SDM-01 is diplayed. Faults on the top of the gas reservoir are mapped in black. This map also shows the three Zeerijp (ZRP) boreholes, which have not been used in this study. Roads and nearby towns are shown for reference. The smaller figure in the top right shows the Groningen gas field in green.

the Groningen area.

Above the Devonian formation we can find a Dinantian age formation (331-359 Ma). The bottom of this formation has been observed in the seismic profiles, but it has not been accurately mapped. This formation consists of a thick carbonate platform (Geluk et al., 2007).

On top of the Dinatian formation the Silesian formation is located. This formation can be divided into three subformations; the Namurian, the Westphalian and the Stephanian (van Buggenum and den Hartog Jager, 2007).

During the Namurian (326-313 Ma), subsidence allowed for the formation of a carbonate basin. The lower Namurian formation originated in a marine environment, and contains black shales. The shallower part of the formation contains more fresh-water carbonates. Faults from below propagate throughout this layer. Because of its organic-rich sediments, the lower Namurian acts as a source rock for natural gas.

During the Westphalian (313-304 Ma), subsidence still took place, and produced high sedimentation rates. The Westphalian contains 4 subsections van Buggenum and den Hartog Jager (2007); the Westphalian A contains more shallow water sediments, whereas formations B and C contain sediments from swamps which were intersected with rivers. The Westphalian D is characterized by its observable change from a tropical to a semi-arid environment. Due to uplift during the entire Westphalian the facies gradually changed from a watery environment to a more dry, floodplain environment.

The Stephanian has only been identified in two Dutch wells, and has been noted to contain red fluvial sediments similar to Westphalian D.

Above the Silesian formation we find the Permian age (299-251 Ma) sediments, which can be subdivided in the Rotliegend and the Zechstein formation (Geluk, 2007b).

The Rotliegend (299-269 Ma) is a sandstone formation. This Permian age sandstone is very porous and acts as a reservoir for natural gas. The base of the Permian is characterized by the Permian unconformity. The base Rotliegend varies in depth throughout the Netherlands, and is even absent in the Texel-IJsselmeer high. The Lower Rotliegend contains more volcanic and clastic rocks, whereas the Upper Rotliegend contains finegrained rocks and evaporites.

Overlying the Rotliegend is the Zechstein formation. This 269-251 Ma evaporite layer acts as a caprock that prevents gas from escaping the reservoir. The composition of this formation alters between marine evaporates and it contains high velocity anhydrite layers. The Zechstein formation is ductile in nature, and faults from below terminate in this formation.

Above the Permian formations, the Triassic (251-200 Ma) formation is found (Geluk, 2007c), which

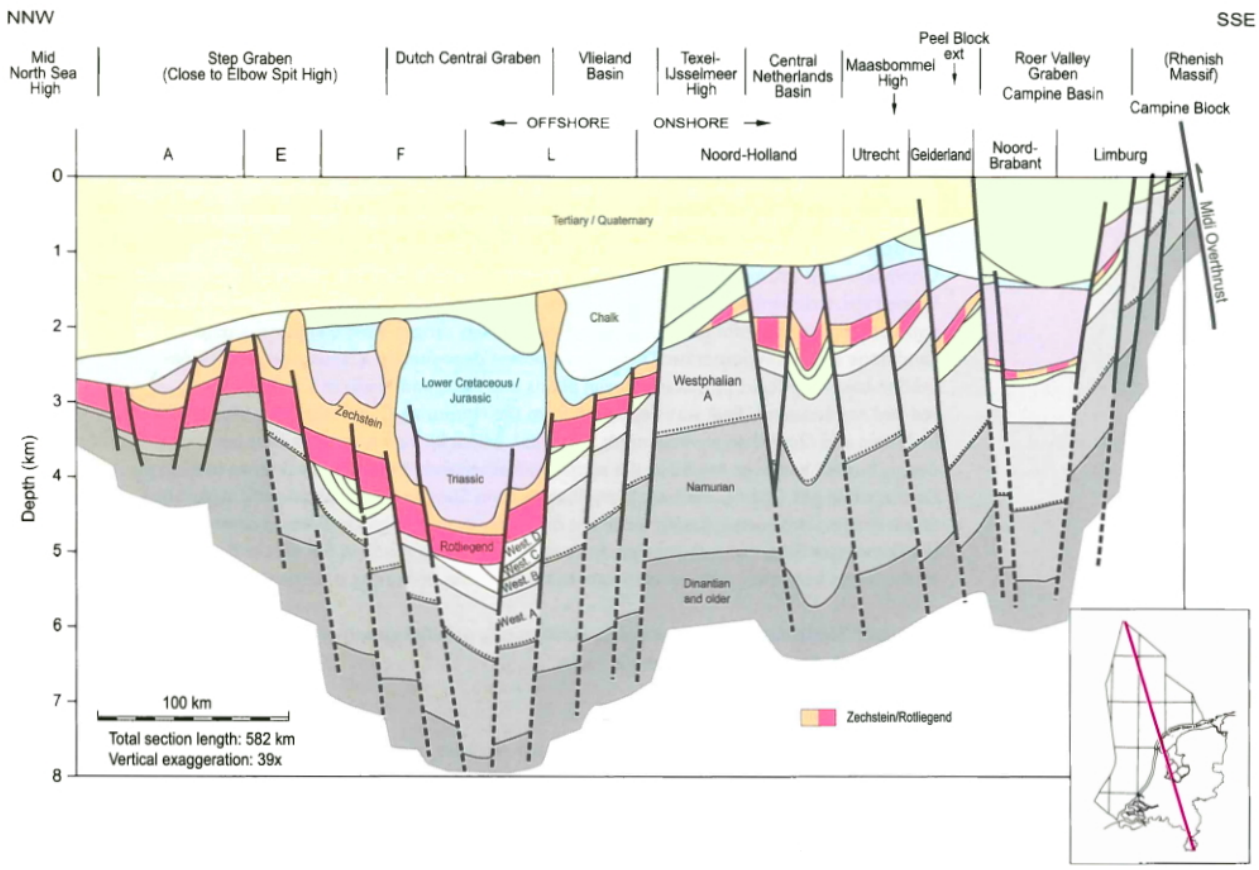

Figure 1.2: Cross section from South Limburg to the Northernmost Point of the Dutch North Sea (van Buggenum and den Hartog Jager, 2007).

contains fine-grained siliclastic deposits from lacustrine environments. Besides siliclastic rocks it also contains carbonates and evaporites. The Triassic formation contains the second largest hydrocarbon reservoir in the Netherlands and is also a source of rock salts. Salt diapirism from the Zechstein formation punctures the Triassic in some regions.

The Jurassic (200-145 Ma) consists of four groups, where the first is of a uniform clay and marine composition, the other three groups are more siliclastic in nature, originating in a more marine, continental and continental-to-marine environment (Geluk, 2007a).

The Dutch Cretaceous (145-66Ma) formation is mainly comprised of the Rijnland and Chalk Groups. These thick formations are the result of rifting during the Cretaceous (Wong, 2007). The Rijnland (145-100? Ma) was deposited in a more fluvial to coastal environment, allowing the deposition of sandstones. The Chalk group (100?-66 Ma) is characterized by deposition of marls and limestones.

Rifting still continued during the Tertiary (66 -2.6 Ma) (Wong et al., 2007b), and mainly consists of marine deposits. At the end of the Tertiary the formation shifted to a more continental composition. The thickness of the Tertiary can be explained by different rates of deposition and erosion in different areas. The top of this formation marks the beginning of the North Sea Group which leads into the Quaternary (de Gans, 2007). The Quaternary is mostly comprised of flat sand gravel and clay at the surface.

The exact composition of the SDM-01 borehole data is described in detail in the DINO LOKET (TNO, 2019).

2 Data

The data were recorded on a geophone array in the abandoned borehole SDM-01. The vertical array consists of ten geophones which measured displacement in three components, the geophones were placed between a depth of 2751 meters to 3017 meters. Data obtained from a continuous recording during the period of October 10th 2013 to December 23rd of 2013 were used in this study. This dataset was previously used in a study of noise interferometry (Zhou and Paulssen, 2017) to constrain the velocity profile of the borehole, and later to study downgoing PS-waves from check shot sources for a more accurate determination of the velocity profile Arwert (2019).

Since the geophones have been placed underground, the amount of recorded noise is lower than if they were place at the surface. When looking at earthquake data recorded on this geophone array, the P-wave arrival can be accurately distinguished.

2.1 Data Extraction

The database of earthquakes occurring in the study period was downloaded from the European-Mediterranean Seismological Center (EMSC) and a database of all the events in the time frame of October 10th to December 23rd was extracted. No constraints were put on magnitude and epicentral distance. This database was then used to extract the events from the geophone data and each event was saved in a separate file. In order to see if these events were useful for this study, each event was sorted on magnitude and distance. Nearby events originating in the Groningen area were obviously recorded. However, these events are too close for PS-conversion to take place, and thus could not be used in the study. Very distant sources from the Fuji Islands, Antarctica, Japan and the Philippines with magnitudes >7 were too distant to be recorded on the geophone array, meaning that a lot of distant events were not fit for this research. One event from Crete, Greece with a magnitude of 6.4 was accurately recorded, but other 6 to 7 magnitude events from the recording period were too distant.

Distant sources with a magnitude of 4 to 6 were mostly not accurately recorded in the data. For example; a magnitude 4.9 source from Western Turkey was not observed. Closer events of magnitude 2 to 4 were recorded however. Useful events for this study were found originating in the North Sea, Germany, France and Poland and one in Liechtenstein. These events showed clear P-wave arrivals. Except for the Crete source, no events with a distance larger than 923 kilometers were used.

Figure A.1 shows the distribution of events with epicentral distance and back azimuth.

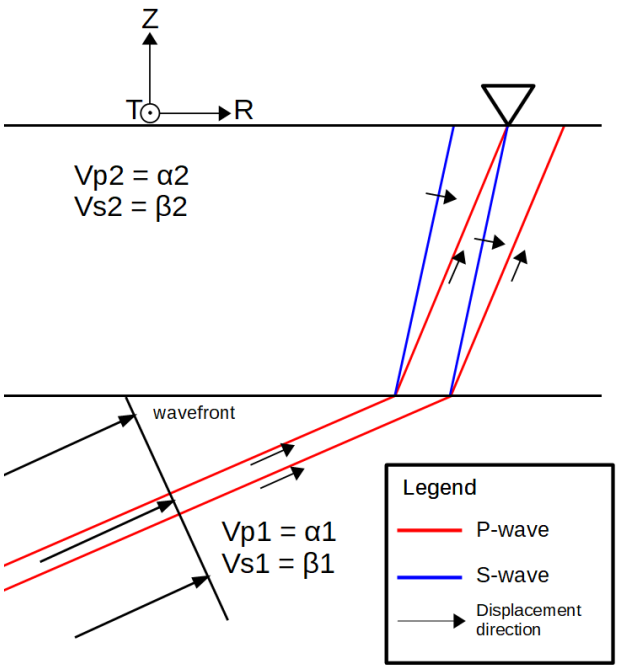

Figure 2.1: A 2 dimensional visualisation of a plane P-wave encountering a horizontal discontinuity, leading to a P-to-S conversion, note that the difference in velocity between the P-wave and the PS-wave leads to a difference in the angle of refraction. For simplicity we ignored P- and PS- reflections and only look at upgoing transmitted waves.

3 Theory

3.1 P-to-S Conversion

When a seismic event occurs, waves start travelling away from the origin in a spherical manner. If the event is observed at a large enough distance from the origin, the wavefront of this source is treated as a plane wave. When studying plane waves, the curvature of the wavefront is neglected.

When a P-wave passes a sharp contrast in density and/or velocity, the transmitted wave will continue travelling in the new medium with a different velocity, this change in velocity determines the angle of refraction of the transmitted wave. In the case of a velocity increase the angle of transmission will be larger than the angle of incidence and in the case of a velocity decrease the angle of transmission will be smaller than the angle of incidence.

Not all the P-wave energy is transmitted, however; part of the P-wave energy is reflected with an angle of reflection that is equal angle to the angle of incidence. The incident P-wave can also excite a displacement perpendicularly to the transmitted P-wave, and a part of the incident P-wave will be converted to a PS-wave.

The transmitted P-wave and the converted PS-wave continue traveling trough second medium at different velocities. If we can determine the delay time between P-, and PS-wave arrival time and know the velocity in the second medium, we can retrieve the depth at which conversion took place.

The P-PS delay time could easily be measured if the source were a short pulse, but in reality this is not the case; the Source Time Function (STF) is usually very complicated and, depending on the type and the magnitude of the earthquake can have a duration of seconds or even minutes (Stein and Wysession, 2009). In most cases, time between the direct P and PS-wave arrival is less than a second, which means that the PS arrival is usually entirely obscured within the P-wave coda, which is the entire signal that comes after the direct P-arrival.

Since the displacements of the P-wave and the PS-wave are perpendicular, the two different wave phases are predominantly recorded on perpendicular components of a 3-component geophone. In a two dimensional problem, the P-wave displacement of a vertically propagating wave is measured predominantly on the vertical Z-axis, whereas the PS-wave is mainly recorded on the horizontal X-axis. In a two dimensional situation the X-axis is parallel to the surface and the propagation direction of the PS-wave is also along the horizontal direction.

If we were to perform a water level deconvolution (section 3.2) on the P-wave coda of two perpendicular components, we would filter out the source time function and the instrument response. This would leave us only with the structural response, which describes the response due to the structural effects. By doing a de-

convolution over the P-wave coda in two components, we would obtain a receiver function, which contains the normalized P-wave arrival of a source and its delayed PS-waves.

In reality, the medium that we study is three dimensional, which means that simply doing a deconvolution over the vertical and horizontal component as in figure 2.1 is not ideal. The 3-component geophone records data on the North-South, East-West, and the vertical Z-direction. In a 3-component geophone the P-wave is mainly recorded on the vertical component of the geophone, and the PS-wave will be distributed over the two horizontal directions. Because the wavefront reached the geophone with a certain angle, the PS-wave is partly recorded on the N-S component and partly on the E-W component. If we convert the NEZ coordinate system to the RTZ coordinate system (Radial, Tangential and Vertical), then we, in essence, convert a three dimensional situation to a two dimensional situation. In the RTZ coordinate system, the radial axis is horizontal and perpendicular to the wavefront, and the RZ plane contains the direction of PS-wave propagation. By rotating to the RTZ coordinate system, the PS-wave will be mainly visible on the radial component and absent on the tangential component. The exact method of rotation is described in more detail in section 3.3.

3.2 Deconvolution

In order to obtain a receiver function we do a deconvolution between the radial signal D_r and the vertical signal D_z. This will give us a function which only contains the structural response.

We can describe the geophone data in the vertical direction as a convolution between three functions:

$$D_z(t) = I(t) \circledast S(t) \circledast E_z(t) \tag{3.1}$$

Where $D_z(t)$ is the recorded data, $I(t)$ describes the instrument impulse response, $S(t)$ is the source time function, and $E_z(t)$ describes the vertical structural impulse response and $\circledast$ denotes the deconvolution (Langston, 1979).

In contrast to the relatively straightforward impulse and structural response, the source time function $S(t)$ can be very intricate and can depend on the magnitude and slip mechanism of the source (Stein and Wysession, 2009).

Doing a convolution in the time domain is a fairly simple operation. Doing the opposite in the form of a deconvolution is a lot less simple.

If we want to deconvolve a signal, we can make use of the convolution theorem, described in Katznelson (2004), which states that a convolution in the time domain can be written as a multiplication in the frequency domain.

If we apply a Fourier transform

$$D_z(f) = \int_{-\infty}^{\infty} D_z(t) e^{-i2\pi ft} dt \tag{3.2}$$

and apply the convolution theorem, we can rewrite equation 3.1 as:

$$D_z(f) = I(f) \cdot S(f) \cdot E_z(f) \tag{3.3}$$

In the frequency domain the convolution operators have been replaced by a multiplication.

We can now describe our function for the receiver function in the frequency domain as follows:

$$RF(f) = \frac{D_r(f)}{D_z(f)} \tag{3.4}$$

By filling in the values for D_r and D_z, we rewrite equation 3.4 as

$$RF(f) = \frac{I(f) \cdot S(f) \cdot E_r(f)}{I(f) \cdot S(f) \cdot E_z(f)} \tag{3.5}$$

here the source time function and the instrument response cancel out and we are left with only the structural response:

$$RF(f) = \frac{E_r(f)}{E_z(f)} \tag{3.6}$$

D_z contains the direct P-wave arrival and D_r contains most all the converted waves, thus we imply $E_z(t) \approx \delta(t)$ and E_r is treated as a function containing the converted waves.

In theory, equation 3.6 gives an answer for the problem. Applying this method in practice is more complex: when the denominator reaches values close to 0, the answer of the receiver function would become extremely large. For this reason we multiply the value of the the receiver function by the complex conjugate of D_z as follows

$$RF(f) = \frac{D_r(f) D_z^*(f)}{D_z(f) D_z^*(f)} = \frac{C_{rz}(f)}{C_{zz}(f)} \tag{3.7}$$

where C_{rz} denotes the cross correlation of D_r and D_z, and C_{zz} denotes the autocorrelation of D_z. By multiplying by the complex conjugate of D_z we ensure that no complex values are present in the denominator, since $D_z D_z^* \in \mathbb{R}$.

This step still does not ensure that the denominator is larger than 0 at all values of the receiver function, thus, in order to prevent low values for the denominator we replace the autocorrelation of D_z with the function $\Phi(f)$

$$RF(f) = \frac{D_r(f) D_z^*(f)}{\Phi(f)} \tag{3.8}$$

with

$$\Phi(f) = max\{D_z(f) D_z^*(f), \varepsilon \cdot max[D_z(f) D_z^*(f)]\} \tag{3.9}$$

where $\varepsilon \cdot max[D_z(f) D_z^*(f)]$ is the water level.

ε is the fraction of the maximum value of $C_{zz}(f)$ that is added to the frequency spectrum. In this research, a value of $\varepsilon \approx 0.1$ yielded good results. When a higher value of ε is taken, important data will be removed from the signal, and a with a lower value too much noise will be included in the deconvolution. A visualization of the water level and its relation to the frequency spectrum can be seen in figure 3.1 (left).

In order to remove additional noise from the geophone recordings, we apply a low pass Gaussian filter in the frequency domain, as described in 4.1, this gives us the final formula for the deconvolution in the frequency domain:

$$RF(f) = \frac{D_r(f) D_z^*(f)}{\Phi(f)} G(f) \tag{3.10}$$

The quality and amount of detail in the receiver function can be changed by adjusting the width of the Gauss filter influencing the amount of frequencies included in the receiver function. The influence of the

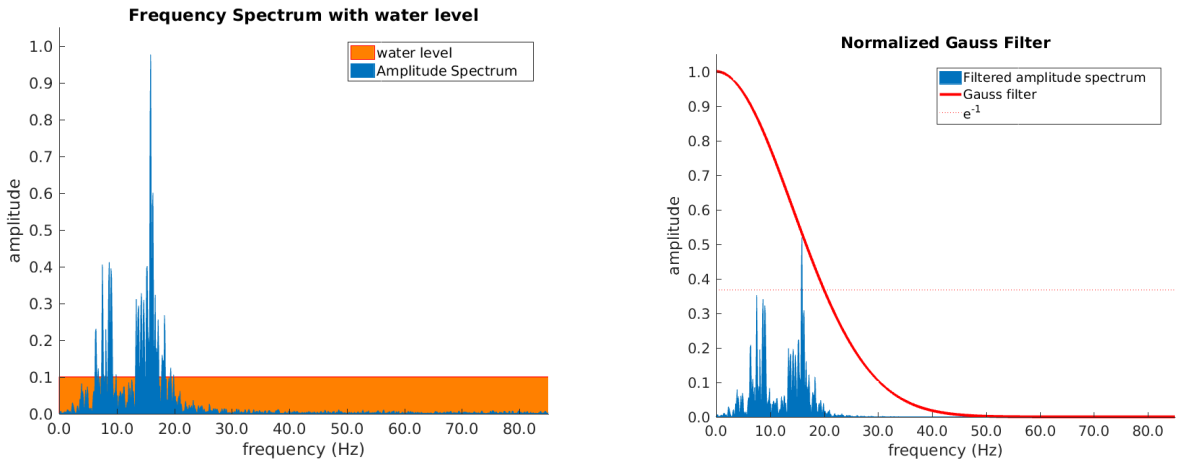

Figure 3.1: (left) A water level deconvolution with a value of 0.1 of the maximum value of the frequency spectrum. (right) The effect of low pass Gauss filtering takes out the higher frequencies out of the frequency spectrum.

Gaussian filter on the frequency spectrum can be seen in figure 3.1 (right).

We can obtain the receiver in the time domain by applying an inverse Fourier transform

$$RF(t) = \int_{-\infty}^{\infty} RF(f) e^{i2\pi ft} df \tag{3.11}$$

We can also influence the length of the data array used in the deconvolution. We define the time window as the amount of seconds after the direct P-wave arrival. We change the time window because the length of the P-wave coda influences the final shape of the receiver function. Using a short time window after the P-wave arrival means that we do not include too many conversions and reflections. With a longer window, more noise and additional phases might be included in the window, which could distort the signal. As mentioned before, small magnitude events have a shorter source time function. Thus for small magnitude sources a shorter wave window is required. Large magnitude events have a longer source time function and a larger window has to be taken. For most sources used, a time window of 5 seconds proved adequate. However, for the Greece event with $m_w = 6.4$ a 15 seconds was used.

3.3 Rotation

As mentioned before, when a PS-wave is recorded at a geophone, it is measured primarily on the horizontal component. Depending of the incoming direction of the wavefront, the displacement is partly recorded on the North-South horizontal component and partly on the East-West horizontal component. An example of a wave approaching a geophone at an angle is visible in figure 3.2, if we want to isolate the displacement on only *one* horizontal component, we need to rotate the geophone coordinate system from the NEZ coordinate system to the RTZ coordinate system. The radial component is perpendicular to the wavefront meaning that the PS-wave will be visible primarily on the radial axes.

Before we can rotate the geophone data from the SDM-01 borehole to the RTZ coordinate system, the geophone data has to be corrected from its arbitrary XYZ coordinate system to the NEZ coordinate system. By recording check shots from known locations around the SDM-01 borehole, the deviation from the horizontal and vertical axes could be determined (Arwert, 2019). The orientation of each of the 10 geophones are given in table 3.1.

We can rotate the geophone data using rotation matrices and these orientations. In this method, the amplitude of the signals is kept equal, but redistributed in the proper direction as if it were recorded on a NEZ coordinate system.

When constructing rotation matrices, we need to take into account that the geophones in the SDM-01 borehole record displacement in a left handed coordinate system (see figure 3.3). Each individual geophone then has to be rotated with the angle it makes with the horizontal as follows

$$\begin{pmatrix} \mathrm{N} \\ \mathrm{E} \\ \mathrm{Z_{inc}} \end{pmatrix} = \begin{pmatrix} \cos(\phi) & -\sin(\phi) & 0 \\ \sin(\phi) & \cos(\phi) & 0 \\ 0 & 0 & 1 \end{pmatrix} \begin{pmatrix} \mathrm{X_{rot}} \\ \mathrm{Y_{rot}} \\ \mathrm{Z_{inc}} \end{pmatrix} \quad (3.12)$$

where the angle between the N-S axis and the X axis is denoted as ϕ.

Due to the close to vertical orientation of the Z-axis we equate $Z_{inc} \approx Z$.

Finally, if we want to rotate the trace data to the RTZ coordinate system we rotate by the back azimuth γ

$$\begin{pmatrix} \mathrm{R} \\ \mathrm{T} \\ \mathrm{Z} \end{pmatrix} = \begin{pmatrix} \text{-}\cos(\gamma) & \text{-}\sin(\gamma) & 0 \\ \sin(\gamma) & \text{-}\cos(\gamma) & 0 \\ 0 & 0 & 1 \end{pmatrix} \begin{pmatrix} \mathrm{N} \\ \mathrm{E} \\ \mathrm{Z} \end{pmatrix} \quad (3.13)$$

Note that here the signs of the cosines in equation 3.13 are opposite to those in equation 3.12, because the angle of the back azimuth is in the opposite direction to the deviations of the geophones.

Depth (m)	Z_{inc}(°)	x_{rot}(°)	y_{rot}(°)
2751.0	15.7	281	11
2780.1	13.8	206	296
2809.5	12.0	325	55
2838.9	10.7	300	30
2868.6	9.0	293	23
2898.2	8.4	318	48
2928.0	7.6	203	293
2957.7	6.8	319	49
2987.6	6.4	326	56
3017.4	5.7	61	151

Table 3.1: The orientations of the 10 geophones during the period the data was recorded, Z_{inc} is the inclination angle, and x_{rot} and y_{rot} are the deviations from the North and the East respectively. Arwert (2019)

We can now visualize the geophone data to see if our rotation was successful. A visualization of an event in the North Sea can be seen in figure 3.4. This event took place at ~300 km distance from the borehole. When the source is close to the receivers, or high in magnitude, the first P arrival can be distinguished very clearly (figure 3.4 (left)). Note that the wavefront is measured at a later time in shallower geophones, indicating that this is an upgoing wave.

We also expect the S-wave to be visible on the tangential component. The S-wave arrival here is expected to arrive at ~80 seconds. In figure 3.4 (right) one can see the S-wave arrival. Since the S-wave arrives later in the wave train, a lot of 'contamination' from other waves is visible in the seismogram.

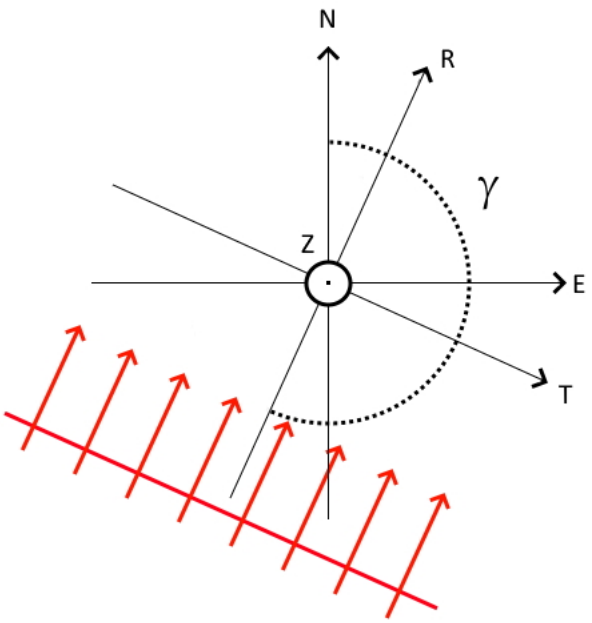

Figure 3.2: The back azimuth γ is the angle of the propagation direction the wavefront (the red line) makes with the station, so for this example, the wave comes from the southwest, meaning that $180° < \gamma < 270°$. The radial axis points along the direction of propagation, and the tangential component is parallel to the wavefront.

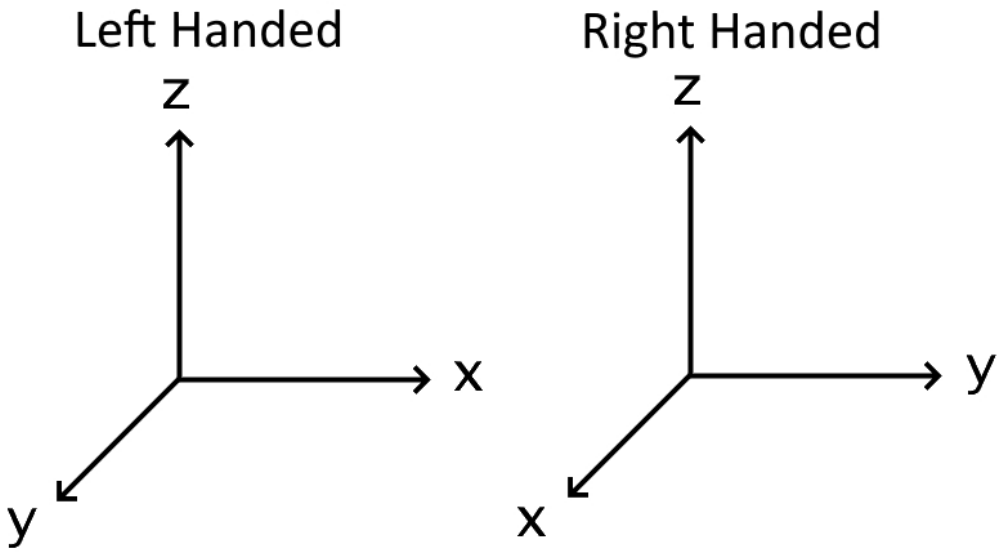

Figure 3.3: In a left-handed coordinate system the X axis makes a 90 degree angle clockwise with the Y axis and the Z axis is pointed upwards. In the right-handed coordinate system the angle between the X-axis and the Y-axis is 90 degrees counterclockwise.

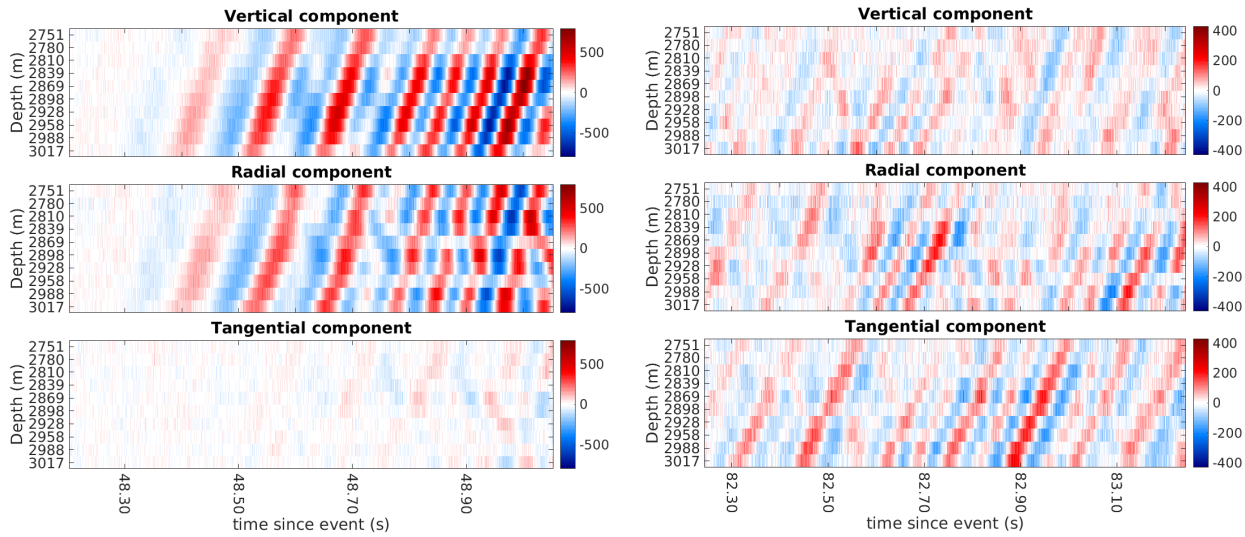

Figure 3.4: (left) Data from a North Sea event, ID: 340633. When the 3-component geophone data is converted to the RTZ coordinate system, the P-wave arrival is clearly visible on the vertical and radial component and is absent on the tangential component. (right) Data from the same event. In the RTZ coordinate system, S-wave arrival is visible on the tangential component and absent on the vertical component. Note that while P arrival on the tangential component does not show any displacement, at the S arrival, the radial and vertical component show signals caused by reflections from the P-wave, or possibly even SP conversions.

4 Methods

The receiver functions were obtained by using the method described in Langston (1979). After the receiver functions were obtained, synthetic data based on one dimensional elastic wave modeling was done to see if similar results could be obtained. With the synthetic data, the goal was to find a model that produced similar results to the real data.

The program was developed by Wapenaar (2019), the deconvolution and filtering have all been performed in `MATLAB`.

4.1 Filtering

Different filters were used to see what gave the best results. In the paper by Langston, a Gaussian filter was used.

The Gaussian in the frequency domain is defined follows:

$$G(f) = e^{-f^2/4\alpha^2} \tag{4.1}$$

The Gaussian filter is a low pass filter which preserves the low frequencies and removes the higher frequencies. Another quality of the Gaussian filter in the time domain is that its Fourier transform is also a Gaussian in the frequency domain.

A different type of filter that has been experimented with is the band pass filter, which could be used to also filter out low frequencies. However, if slope of the filter is too steep, 'ringing' of the signal will occur when converted back to the time domain.

The low pass Gaussian filter was preferred. While this filter does not remove very low frequencies, the low frequencies did not significantly influence the final deconvolution results.

The behaviour of the Gaussian filter can be described as follows; if f is equal to 2α, then

$$G(2\alpha) = e^{-(2\alpha)^2)/4\alpha^2} = e^{-1}$$

In figure 3.1 we see that the value of $G(f)$ equals e^{-1} at 2α and approaches zero when $f = 5\alpha$.

Since the geophones used in this study are most sensitive at a values between 5 and 20 Hz (see figure 3.1) we use an alpha value of 10 Hz. This way, signals above 50 Hz will disappear and most frequencies above 30 Hz will be diminished by a factor 0.1.

4.2 Velocity Relations

The P-wave velocity profile throughout the entire borehole is accurately constrained from a sonic log (TNO, 2019). However the S-wave velocity and density of the borehole are not known. In this section we describe how the S-wave velocity and the density were determined from the P-wave velocity.

A substantial amount of studies were done to determine the relationship between P- and S-wave velocities and the densities of certain lithologies. By studying borehole logs, seismic profiles and other velocity

measurement methods, Brocher (2005) derived equations to explain relationships between velocities and densities.

Brocher used the Nafe-Drake curve, an empirical 5th order polynomial, which describes the relationship between P-wave velocity and density, and compared it to linear relationships found in experimental data. It was concluded that the Nafe-Drake equation adequately described the relationship between P-wave velocity and density:

$$\begin{aligned} \rho\,(\mathrm{g/cm^3}) = 1.6612V_p - 0.471V_p^2 \\ +0.0671V_p^3 - 0.0043V_p^4 + 0.000106V_p^5 \end{aligned} \tag{4.2}$$

Brocher also used observed data to obtain a relationship between S and P velocity, which he calls "Brocher's Regression fit"

$$\begin{aligned} V_s = 0.7858 - 1.2344V_p + 0.7949V_p^2 \\ -0.1238V_p^3 + 0.0064V_p^4 \end{aligned} \tag{4.3}$$

For a given P-velocity profile, a model based on these two functions with realistic values for V_p and ρ could be constructed.

In figure 4.1 we can see the relation between P-wave velocity with densities and S-wave velocity.

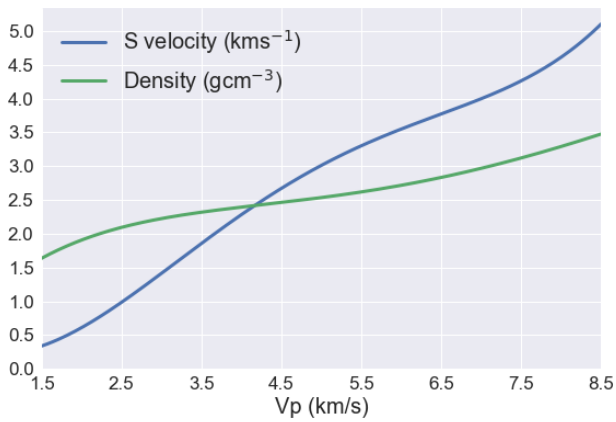

Figure 4.1: The relationship between Vp and Vs and the relationship between Vp and ρ from formulas 4.3 and 4.2.

4.3 Elastic1d

In order produce synthetic data, we used the *elastic1d* MATLAB code, stemming from the exploration geophysics group of Kees Wapenaar, TUDelft. With this program, the behaviour of P and S plane waves traveling through a 1D medium can be simulated. The user can provide a 1D velocity model, after which the program calculates reflection coefficients for each interface as defined in Aki and Richards (2002). These reflection coefficients describe how an incident wave is converted, reflected and transmitted, and are described in more detail in appendix B. These coefficients rely on the slowness of the plane wave and the P-, and S-velocities above and below the interface. Using the P- and S-wave velocities, the travel times of each phase throughout each medium are computed and a model response is generated.

In figure 4.2 we can see the borehole P-wave velocity profile and the estimated 1D model with the layer transitions. Instead of modeling the response of the exact borehole profile, an average velocity for each formation was used for the input model, since using the exact borehole velocity profile as an input model would drastically increase processing time.

Beside the wave velocities and densities, an input slowness also needs to be provided. This horizontal slowness s of the wave describes the relation between the angle of incidence i and wave speed v: $s = \frac{sin(i)}{v}$. When an event occurs at a large epicentral distance, its slowness is large, a higher slowness value corresponds to more horizontal propagation.

Seismograms are then calculated for the entire depth range of the model so the displacement of P-waves and S-waves over time can followed over the entire depth profile.

The original *elastic1d* works with a wave originating from the surface, thus it cannot directly be used to model upgoing waves coming from below. Therefore the entire input model was inverted in order to simulate upgoing waves.

The program also asks for a source time function. Here we have chosen to use a Ricker wavelet with a dominant frequency of 15 Hz, since this was the dominant frequency of most earthquake sources used in this study.

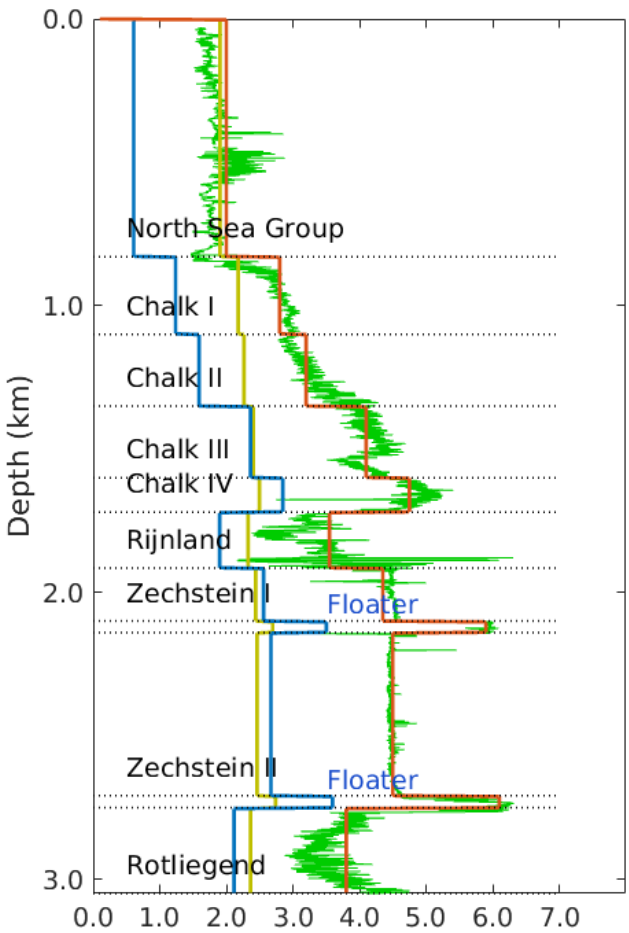

Figure 4.2: Based on the well log data (the green line) a rough velocity profile has been inferred in red. The corresponding S-wave velocity can be seen in blue and the corresponding density is plotted in yellow-green. The formations are based on those described in van Weers (2019)

4.3.1 Validity for a Simple Model

In order to verify the validity of the *elastic1d* code, a two layer model has been made, as in image 2.1. The velocities used for the simple 2 layer model describe a low velocity formation at the top and a high velocity formation at the bottom, with the values given in table 4.1. The resulting wave fields are shown in figure 4.3, seismograms have been calculated for the vertical and the radial displacements. As expected, we see (1) a decrease in P-wave velocity, (2) a converted S-wave which travels slower than the transmitted P-wave, and (3) a reflected P and a reflected PS-wave, all originating at a depth of 1.25 km, the depth where the discontinuity was placed.

The polarities of the two wave fields agree with the reflection and transmission responses predicted by Aki and Richards (2002). Now we can obtain receiver functions from these data. For each trace depth, a receiver function has been determined using the method described in section 3.2. The calculated receiver func-

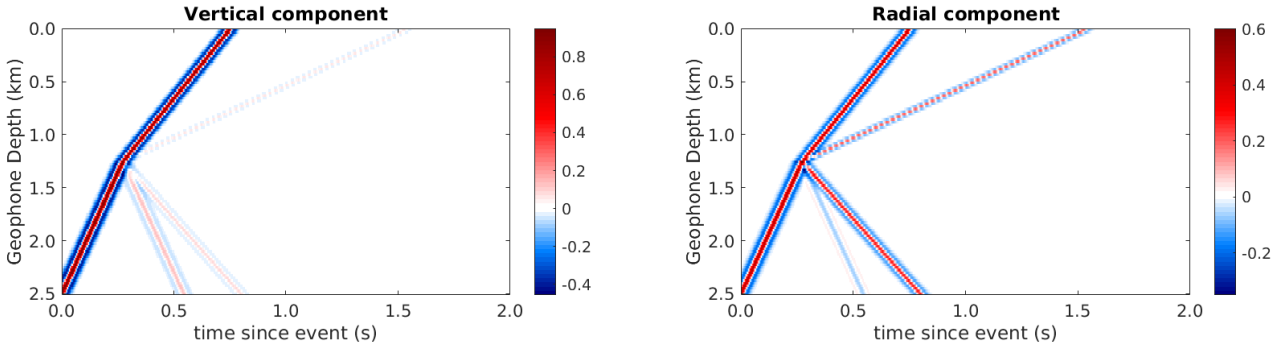

Figure 4.3: In this figure the direct P and P conversion can be seen, as well as the direct reflection and the PS-reflection. We used the 2 layer model from table 4.1 and an input slowness of 13.6s$^{\circ -1}$. Notice that the P-wave has a higher amplitude and the PS-wave has a lower amplitude. The PS-wave is more visible on the radial component.

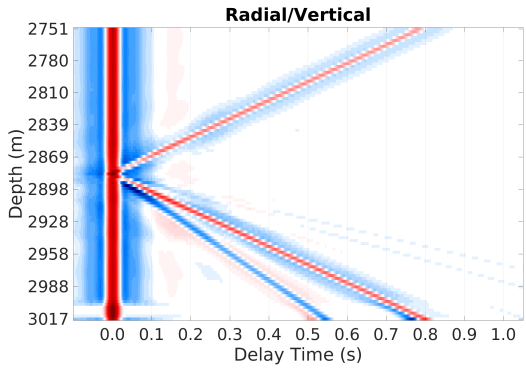

Figure 4.4: After performing a water level deconvolution of the data of figure 4.3 the P-wave is centered at 0 seconds, and the delay between the P-wave and its reflections and conversions at different depths can be obtained.

tions can be seen in figure 4.3. Here we see that the P-wave has been normalized at $t = 0$, and that the conversions can be seen as a delay with respect to the P-wave time. This cross section shows that the *elastic1d* program can be used to model PS-conversions.

d(km)	Vp(kms^{-1})	Vs(kms^{-1})	$\rho(gcm^{-3})$
1.25	2.5	1.0	2.1
2.50	4.0	2.3	2.4

Table 4.1: The values used to generate the data in figure 4.3 and 4.4.

The *elastic1d* program can accurately model wave conversion and reflection. These wave fields can also be used to make receiver functions, which means that this method can be applied to model the 1D structure below the Groningen gas field.

4.3.2 Model Variables

Now that the approach has proven to be accurate for a two layer model, we can continue by working with a more complicated model. If we want to create a model of the borehole down to the reservoir, we can use the P-wave velocity found from the well log data as visible in figure 4.2. Strong discontinuities in the shallow geology means that strong downgoing reflections will be generated. These downgoing waves in themselves do not pose too much of a problem. Unfortunately, the *elastic1d* code does not take into account attenuation. This means that the amplitude of reflected waves from shallower layers will be larger than in reality, and these reflected waves overprint the converted upgoing PS-waves. For this reason, sharp contrasts in the model have been reduced, while keeping in mind that the average velocity must still be equal to the average velocity of the true velocity profile.

The deeper geology is largely unknown. The change in arrival time of upgoing waves is influenced by the depth of the discontinuity and the velocity below the reservoir.

Because discontinuities can be placed at different depths we can identify the different arrivals in the actual data and compare this to the synthetic data. If the receiver functions contain multiple delayed arrivals, then this means that multiple discontinuities have to be added in the model to reproduce these later arrivals.

In order to identify these different arrivals, experimentation with slowness and layer depths need to be done. Since most used sources have a slowness of roughly 0.117 s/km, we can also try to see if there is a

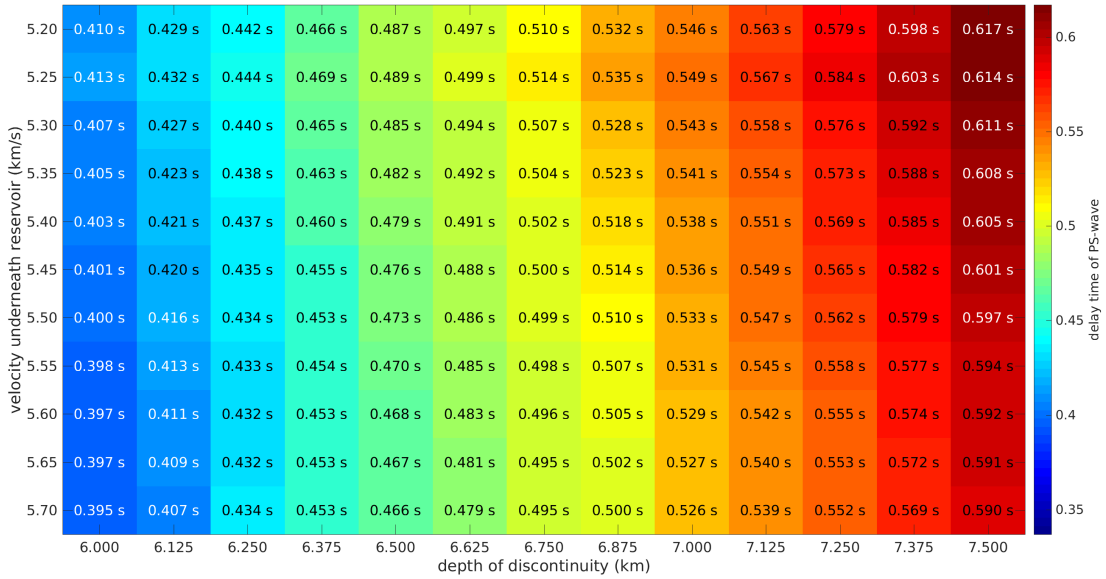

Figure 4.5: Difference in synthetic PS-wave delay time when changing the depth of the discontinuity and the velocity below the reservoir.

difference in arrival time caused by lateral heterogeneity.

4.4 Results of elastic1d

After the velocity model of the borehole (0-3 km depth) was simplified and after the different lithologies were identified (figure 4.2), the only unknowns that remained was the discontinuities below the reservoir.

In order to reproduce the best results, first the shallowest layers beneath the borehole were added, and deeper layers have been added subsequently. Because the shallow converted waves only traverse one formation, and deeper conversions travel through multiple layers, the arrivals of the deeper converted PS-waves are influenced by all of the above lithologies.

Before adding all the other discontinuities, an analysis model was done to see how the depth of the one discontinuity and the velocity of the layer affect the arrival time of the converted S-wave. The results can be seen in figure 4.5. When adjusting the velocity of the layer, we see that the PS-wave delay time is not significantly affected. When we adjust the depth of the discontinuity we see that there is a much greater influence on PS-wave arrival time. From this we infer that realistic velocity variations of the formation have a smaller effect on the PS-arrival time than the depth of the formation.

After a first rough estimate of the depth of the discontinuity, depth and velocity variation can be fine-tuned to fit the observed data.

We also investigated the effect of the slowness of the incoming wave. The converted PS-wave arrives later when the slowness increases. However, while the arrival time is delayed, the amplitude of the PS-wave increases with increased slowness. This is because a higher slowness increases the amount of P-to-S conversion.

5 Results

5.1 Obtained Receiver Functions

By applying the water level deconvolution method to the data from borehole SDM-01 (section 2), receiver functions have been obtained from fourteen events, which can be seen in figure 5.1.

Table 5.1 depicts all of the events used in this study. In this table the origin time, magnitude and depth of the used events can be found.

In order to accurately determine the length of the P-wave coda, we experimented with different window lengths. By taking a window of 5 seconds, a lot of detail can already be observed. And by filtering the raw data with a Gaussian filter where the value of $\alpha = 10$ Hz, the direct P-arrival becomes more apparent as can be seen in figure 5.2.

The obtained receiver functions for an array of geophones can be seen in figure 5.3. The normalized direct wave can be seen at $t = 0$ seconds. And a delayed wave is coming in at the bottom geophone at $t \approx 0.50$ seconds, a downgoing wave can also be seen at $t = 0$ seconds at a depth of 2780 meters.

While some converted waves can be seen in this one receiver function array, it is hard to distinguish signal from noise. The receiver functions were stacked in order to see if similarities and differences from earthquakes from different epicentral distances and back azimuths could be observed, and if the amount of noise can be diminished.

In this results section we will mostly show stacked receiver functions. In appendix C receiver functions for all the individual events can be seen. There we show the receiver function of each event, with a length of 1 and 3 seconds.

Since the events have different back azimuths and epicentral distances, we use stacking to find similarities and differences between these events.

5.1.1 Identified Phase Arrivals

In most of the receiver functions presented in appendix C, a upgoing wave can be accurately distinguished coming in at the bottom geophone around ≈ 0.5 seconds. The exact timing of this '0.5' second arrival was determined for the individual receiver functions.

As can be seen in table 5.2, the events arriving from different directions showed observable differences. In sources with a back-azimuth of 160°-180° we can clearly see the '0.5' seconds arrival coming in at 0.51 seconds. Events coming from the Southwest and from the East had an average arrival time of 0.50 s, and events coming from the Northwest, with an azimuth of 320° to 345° arrived at the 0.49 second mark.

Events with a similar back azimuth but different epicentral distances did not show any significant difference in arrival times. Therefore in the stacking process, epicentral distance was not taken into account.

5.1.2 Stacking the Receiver Functions

Close events were treated as equal in the stacking process, while more distant events were stacked separately. Note that the large magnitude event from Greece has been left out: Due to its larger distance and magnitude it has lower frequencies than the other events and thus this event could degrade the stacked receiver function.

When stacking the events different regions, we observed no significant dependence on epicentral distance. Thus, only stacking for different back azimuths was applied.

Receiver functions of two North Sea events have been stacked (figure 5.4 top left) as well as two events from France and an event from the Southern North Sea (figure 5.4 bottom left). Another stack includes 3 events from Germany and one from Liechtenstein (figure 5.4 top right). Finally a batch with 3 sources in Poland were stacked with one source from Germany (figure 5.4 bottom right). Again, for the receiver functions used for these stacks, a window of 5 seconds was used, as well as an ε of 0.1 and a Gaussian filter with $\alpha = 10$ Hz.

We see some obvious similarities and differences in figure 5.4. Again, the upgoing wave at 0.5 seconds is very clear, and a downgoing reflection originating at 2809 m depth can be seen. We again see that the upgoing wave at 0.5 seconds arrives slightly earlier in the North Sea stack, and later in the Germany stack. We again see events from the Poland region show an arrival of 0.50 seconds and a similar time was found for events coming from the France area.

Other delayed upgoing waves can be observed at 0.1 seconds (while usually partly overprinted by a downgoing PS-wave), 0.35 seconds, 0.60 seconds and maybe even one at 0.70 seconds. Downgoing waves can also be seen at the top geophone, as well as a strong downgoing wave at around 2.00 seconds and two less significant downgoing waves can be seen at 0.3 seconds and 0.4 seconds.

After the receiver functions coming from different locations were stacked, another final stack was made containing an average of all the stacks in order to see if similarities between all of the receiver functions could

Date	Time	Lat	Long	d	m_w	Region	ID	Δ	γ
2013-10-12	13:11:54	35.56	23.31	47	6.4	CRETE, GREECE	338758	21.27	140.00
2013-10-24	08:32:58	51.39	2.86	1	3.0	NORTH SEA	340633	3.05	231.92
2013-10-28	11:09:19	57.39	2.32	40	2.5	NORTH SEA	341250	4.76	330.18
2013-11-14	05:09:11	51.56	16.12	2	3.5	POLAND	343650	6.02	103.37
2013-11-21	09:53:04	47.68	-2.88	2	4.6	FRANCE	344701	8.32	230.99
2013-11-23	23:15:21	51.52	16.15	2	3.8	POLAND	345140	6.06	103.66
2013-11-30	18:09:57	50.35	7.37	10	2.5	GERMANY	346178	3.02	171.82
2013-12-01	09:48:18	60.69	1.79	10	3.1	NORTH SEA	346399	7.83	342.03
2013-12-02	05:23:27	51.62	6.83	1	2.1	GERMANY	346847	1.72	177.29
2013-12-10	06:23:31	51.44	16.05	2	3.8	POLAND	347501	6.03	104.58
2013-12-12	08:02:41	49.62	0.19	1	3.2	FRANCE	347777	5.51	230.16
2013-12-12	06:02:49	47.06	9.48	3	2.0	LIECHTENSTEIN	347769	6.53	163.04
2013-12-16	02:09:24	51.57	6.84	1	2.3	GERMANY	348421	1.77	177.16
2013-12-20	19:57:00	52.83	8.15	5	2.4	GERMANY	349422	1.01	119.47

Table 5.1: Table listing all events used in this study, sorted by event date.
Time is in UTC. Lat Long, is Latitude and Longitude in degrees North-South and East-West Respectively. d = depth in km. m_w is magnitude. Δ is epicentral distance in km, γ = back azimuth in degrees.

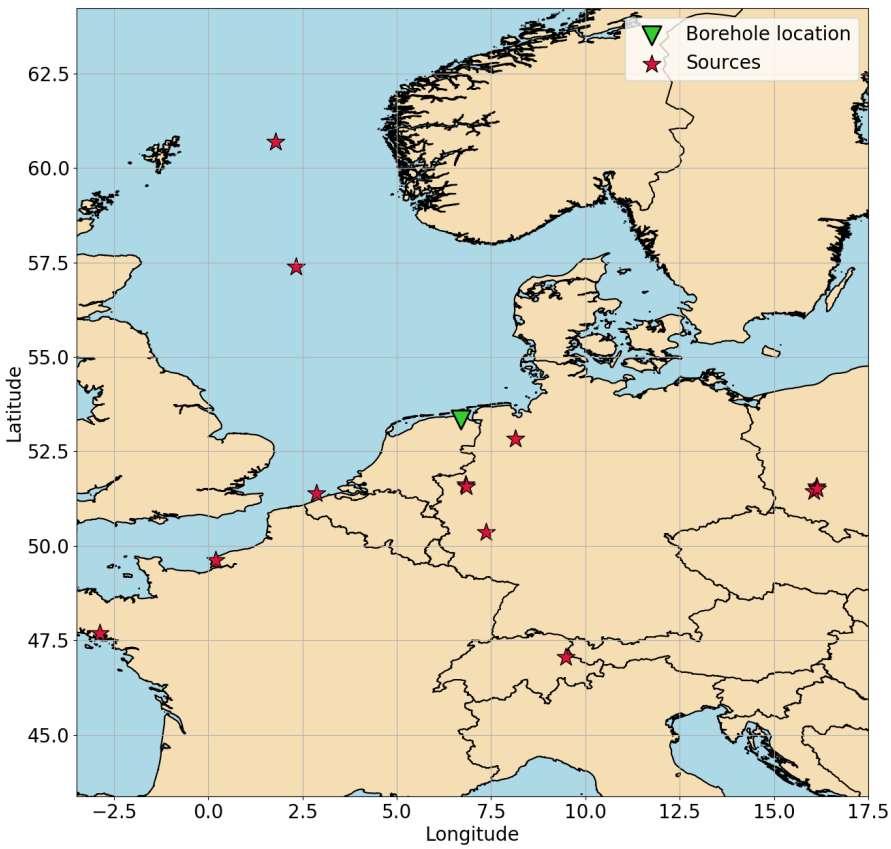

Figure 5.1: Location of the SDM-01 borehole (green triangle) and the earthquakes that were used (red stars). Note that, due to its larger distance, the Greece event has been left out.

be detected. In figure 5.6 the individual upgoing waves at 0.12 seconds, 0.33 seconds, 0.50 seconds and ~0.60 seconds become more apparent. The downgoing reflection at 2809 meters also becomes more prominent in all of the stacks.

5.1.3 Synthetic Comparison

The shallow velocity profile up throughout the entire borehole is very well constrained, so in this study downgoing reflections will be mostly ignored. The focus will instead be put mostly on the upgoing conversions. Thus in the shallow structure discontinuities

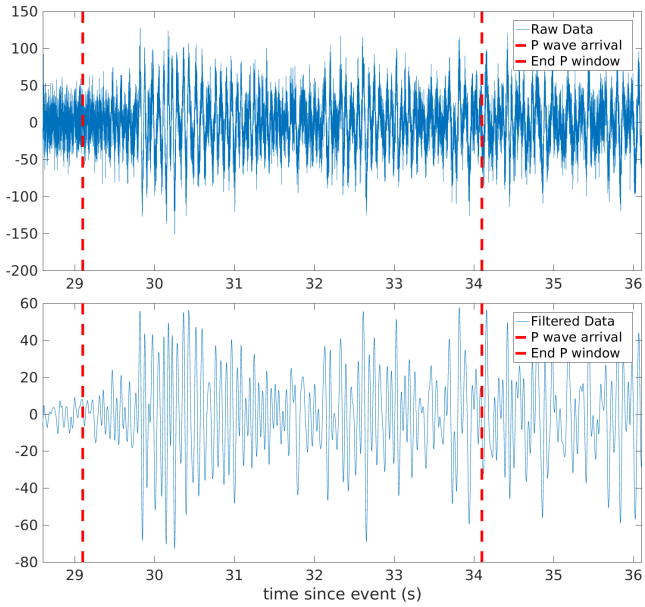

Figure 5.2: The P-wave coda used to obtain an array of receiver functions for an event in Germany (ID = 346847). Above is the raw data, and below is the filtered data, here a Gaussian filter with an α of 10 Hz is used.

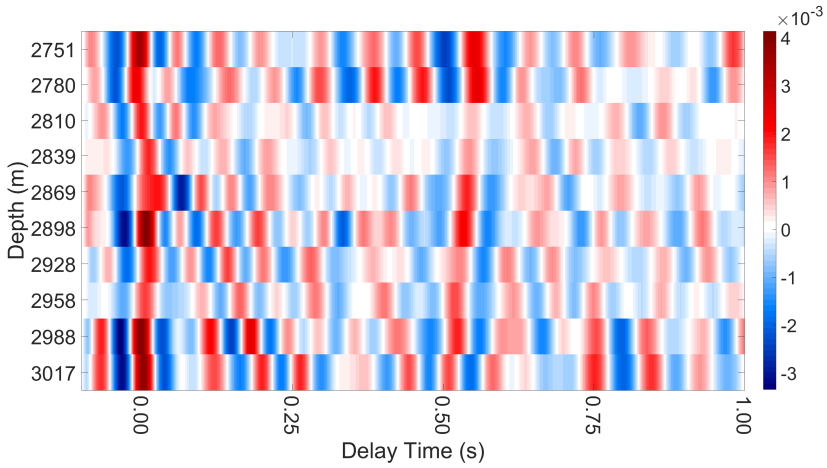

Figure 5.3: Receiver function array of an event in Germany (ID = 346847). Windowsize= 5 seconds, $\varepsilon = 0.1$, $\alpha = 10$ Hz.

have been deliberately subdued.

By placing discontinuities at different depths, as in figure 5.8 we can reproduce the arrivals in the aforementioned data.

Most events had a slowness of ~13s/°, and thus only variation in depth and velocity has been taken into account. It is also important to note is that since this program only works with a one dimensional model, tilted layers can not be modeled.

Four PS-wave arrivals were consistently visible in the observed data, thus four discontinuities have also been placed below the reservoir in the model.

Layers were incrementally added below the reservoir, starting with the formation where the earliest delayed arrival originates and seeing how that agrees with the observed data. Eventually, the 0.12 second arrival has been reproduced by adding a discontinuity at 3.7 km, the 0.32 seconds signal has been reproduced with a discontinuity at 4.7 km. For a discontinuity at depth a 5.85 km we observed an arrival at 0.49 seconds, and with 6.15 km an arrival of 0.51 seconds could be recreated. The depth of this discontinuity should thus fall between 5.85 and 6.15 km. A final discontinuity was added at 6.8 km to replicate the 0.6 second arrival. Due to the observable differing arrival time of the '0.50' second arrival time, the depth and velocity of the formation where this conversion occurs was experimentally examined to see the influence of arrival time, similarily to what was done in figure 4.5.

Keeping in mind that (1) the depth of the discon-

SourceID	Region	BackAzimuth (°)	Delay (s)
340633	NORTHSEA	232	0.49
341250	NORTHSEA	330	0.47
346399	NORTHSEA	342	0.49
338758	CRETE	140	N.A.
347777	FRANCE	230	0.49
344701	FRANCE	231	0.51
346178	GERMANY	172	0.51
346847	GERMANY	177	0.51
348421	GERMANY	177	0.51
349422	GERMANY	119	0.49
347750	LIECHTENSTEIN	163	0.51
345140	POLAND	104	0.45
343650	POLAND	103	0.49
347501	POLAND	105	0.50

Table 5.2: The arrival time of the '0.5' second arrival in different events.

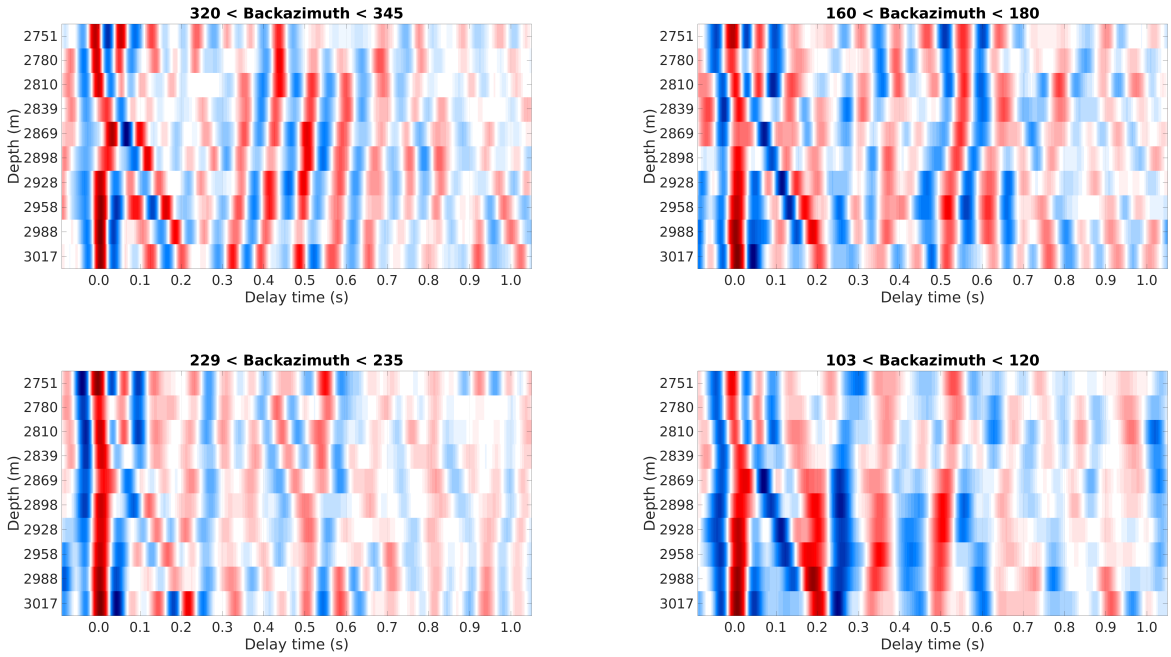

Figure 5.4: 4 stacks of different receiver functions coming from different back azimuths, disregarding the difference in epicentral distance.

tinuity causing the conversion at 0.12 and 0.30 seconds have been pinpointed fairly accurately, (2) the values for the velocities have been kept within a realistic range: between 4.80 km/s, which is the value above the discontinuity and the P-velocity below: 5.20 km/s. We have shown the influence of velocity and discontinuity depth on PS-arrival time, see figure 5.5. From this figure we observe that when the discontinuity is placed between 5.85 and 6.15 km, the '0.5' second PS-wave arrives at the values seen in table 5.2.

In figure 5.8 the final model and its response can be seen. This figure contains tentative names for the formations, which are described in more detail in figure 6.4. Figure 5.7 shows the response at the depth of the geophones. This response can now be compared the arrivals of the average stacks from the observed events in figure 5.6.

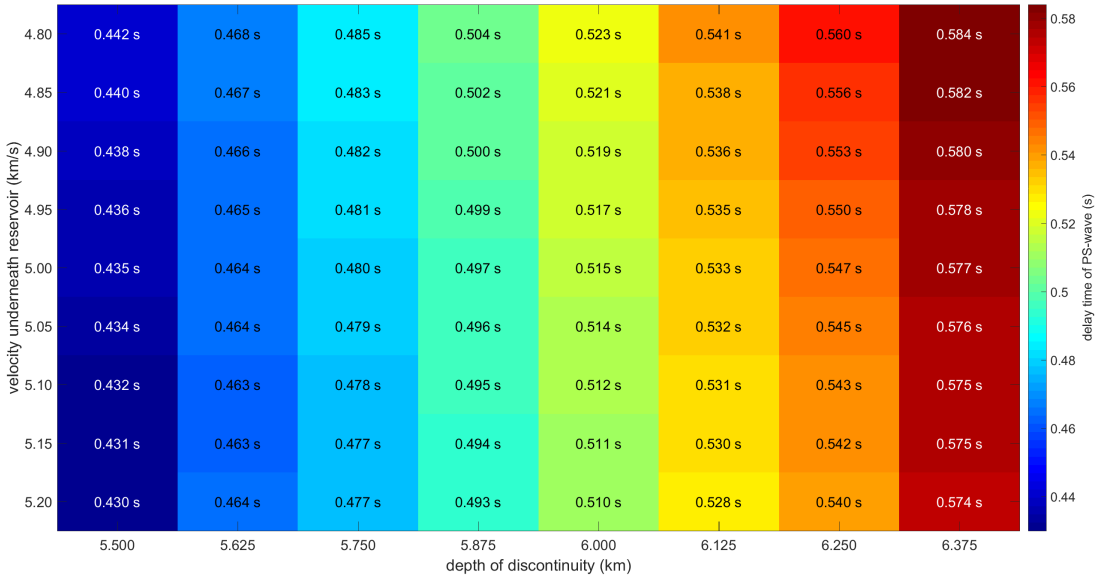

Figure 5.5: The influence on depth of the discontinuity and velocity of the formation on the delay time of the PS-wave.

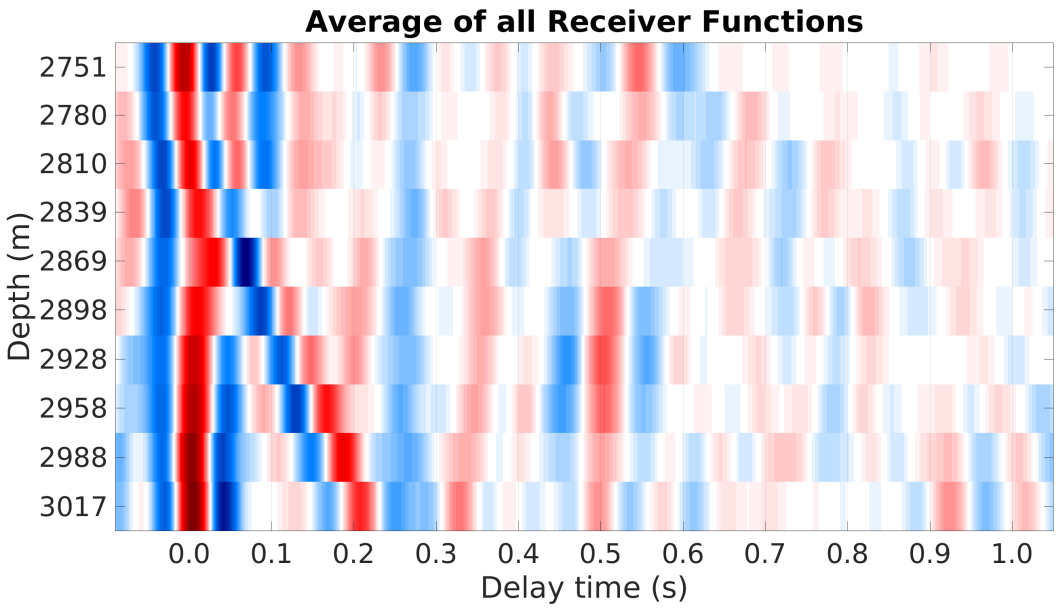

Figure 5.6: Stack of all the receiver functions.

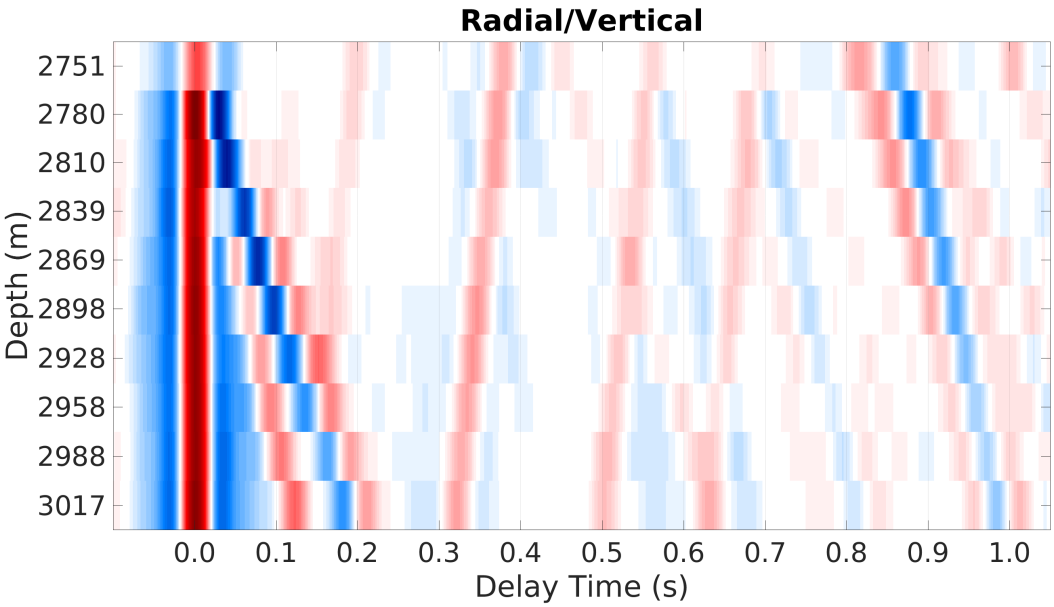

Figure 5.7: The final synthetic receiver functions made with the model presented in figure 5.7, showing conversions coming in at 0.1, 0.3, 0.5 and 0.6 seconds

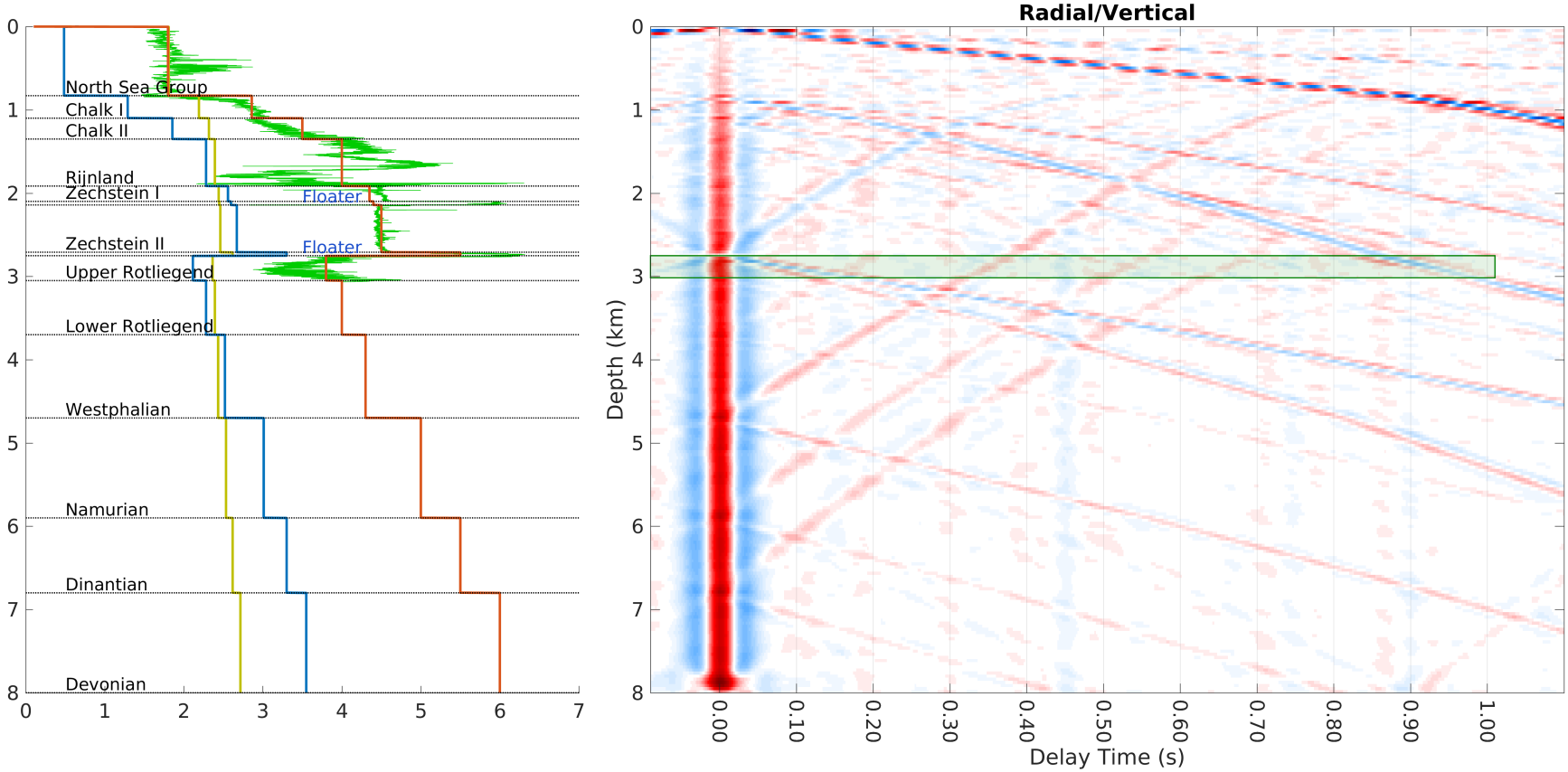

Figure 5.8: (Left) the model used to calculate the wave field. The detail in the shallow model has been reduced in order to diminish downgoing reflections, distorting the upgoing PS-conversions.
Again; The green line shows the P-wave velocity in the borehole the inferred P-wave velocity in red. The corresponding S-wave velocity can be seen in blue and the corresponding density is plotted in yellow-green. (Right) Receiver Function of traces throughout the entire velocity model. The green rectangle shows the location of the geophone array.

6 Discussion

6.1 Interpretation of Results

From the arrival times of the upgoing waves in the receiver functions, we can certainly interpret these waves as PS-waves originating at the discontinuities. The arrivals of the converted PS-waves at 0.5 seconds clearly changes for different earthquake sources. This becomes most apparent for sources with different back azimuths. We see arrivals from the west have a delay time which is earlier than 0.50 seconds. Events coming from the East have a delay time that arrives small bit later than 0.50 seconds. PS-waves coming from the South arrive exactly at 0.50 seconds.

The limited data coverage makes it difficult to accurately constrain the depth of the discontinuities, a larger data set would make it easier to constrain the PS-wave delay time in response to a different back-azimuth and epicentral distance. The current dataset, while convincingly showing that a heterogeneity exists below the Groningen reservoir, does not give us enough information to accurately determine the precise structure below the reservoir.

The obtained data also shows that a number of upgoing PS-waves are overprinted by reflected downgoing waves, which sometimes makes it difficult to accurately distinguish the converted waves. Still, judging from the current receiver functions, converted waves coming after the 0.62 seconds PS-wave are hardly noticeable. This tells us that it is unlikely that the structure below the 6.8 km discontinuity can be explained using this dataset.

From the synthetic tests we can say that the depth of the discontinuity has a strong impact on the arrival of the converted PS-wave, and that the impact of velocity is relatively small, as can be seen in figure 5.5.

6.2 Quality of Results

Although the quality of the results proved to be higher than expected, the quantity of obtained receiver functions did fall short of the expectations. The list of events recorded in the European-Mediterranean Seismological Centre (EMSC) database was initially very promising, as 4487 events occurred in this period. Yet, a lot of the events in this database were not recorded by the geophone array. This can be attributed to the fact that a large number of events were too low in magnitude or too distant to be recorded.

In the end, no more than 14 events were eventually used in this study, which is much lower than initially expected.

Nevertheless, because the quality of the receiver functions outshined the expectations, the converted PS-waves could be distinguished very clearly.

Even though the original goal of the study was to locate a discontinuity at a depth of ~6.0 km, even more PS-conversions have been identified. This suggests that the vertical array receiver function method can be used to model the structure below the reservoir in even more detail than expected. So even though the amount of data is lower than initially anticipated, the quality of the data itself much higher than expected.

6.3 Limitations of the Research

The limited amount of events that were recorded in the geophone array made it difficult to convincingly pinpoint the interfaces below the SDM-01 borehole. The benefit of this limited dataset is that the available events have been thoroughly examined. The mathematical methods that were used did not provide any limitations and all of the calculations operations have been done on middle-end machines, so processing power is not a limitation.

The model gave an accurate explanation for the depth of the discontinuities, however, the model does not take into account tilted layers. Tilted layers could influence the local slowness of an event by changing the propagation angle of the wave. In this research we only took into account a 1D structure. Modeling in 3D is required to model the exact structure including tilted layers, this method could be used to model the change in local slowness.

6.4 Comparison with other Research

The history of the Dutch subsurface is extensively described in 'Geology of the Netherlands' (Wong et al., 2007a). The names that were used for the discontinuities that we identified have been taken from the cross section shown in figure 1.2 and other sections in this book. The discontinuities were tentatively identified as the base of the lower Rotliegend Group at 3.7 km, the Westphalian at 4.7 km, the Namurian at 5.85-6.15 km, and the Dinantian at 6.8 km.

In this book, two formations, named the Silesian and the 'Pre-Silesian', are discussed. The top Silesian has been estimated at a depth of ~2,800 meters (see figure 6.1. This depth contradicts the depth of the base Zechstein Geluk (2007b), which is at a depth of 3,050 m at Stedum. We have thus identified the base of the lower Rotliegend at 3.7 km, and the top Pre-Silesian has been estimated as a depth of 5,700 - 6,000 m, which corresponds with the Dinantian-Namurian discontinuity. Images of these depths are visible in figure 6.1.

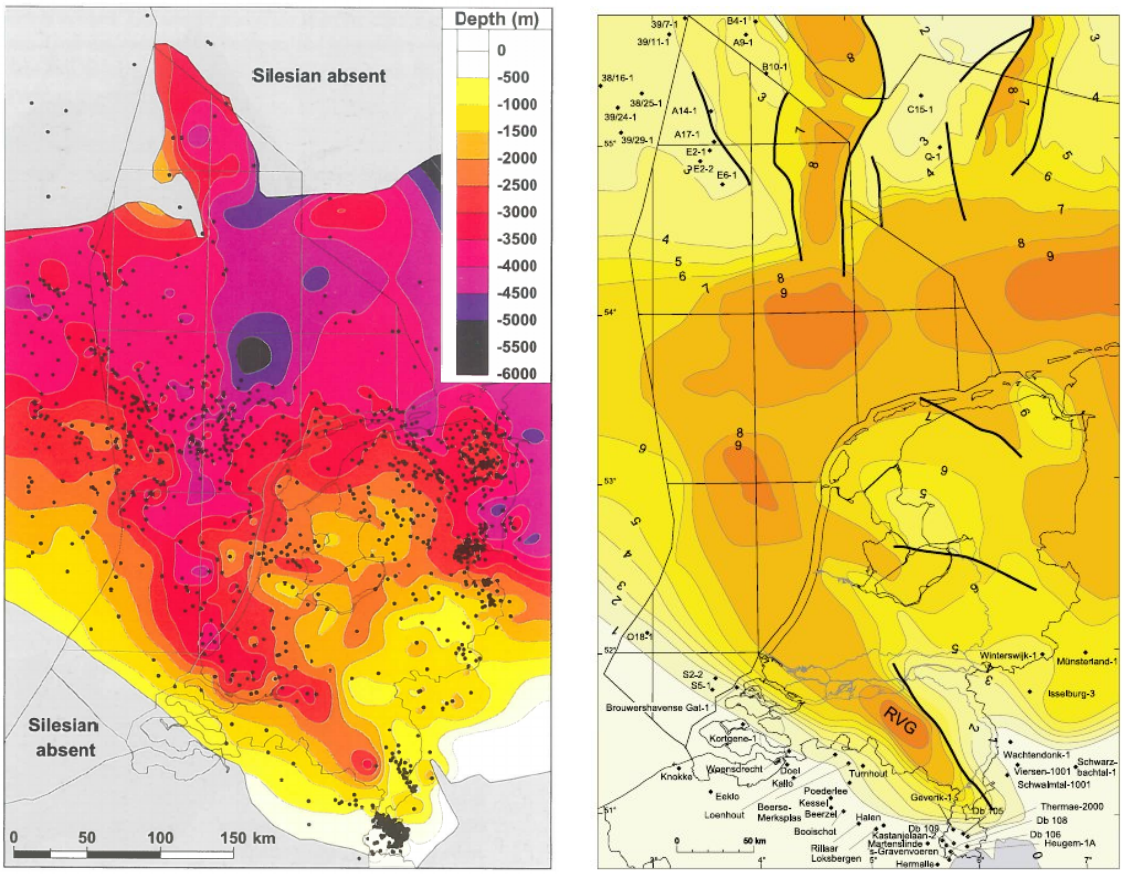

Figure 6.1: (left) The depth of the top Silesian (van Buggenum and den Hartog Jager, 2007) is slightly too shallow to correspond with the depth from the synthetic data. (right) The depth of the top Pre-Silesian (Geluk et al., 2007) has a depth of 5.8-6.1 around Stedum, corresponding with the discontinuity causing the ~0.5 second delay in the synthetic data

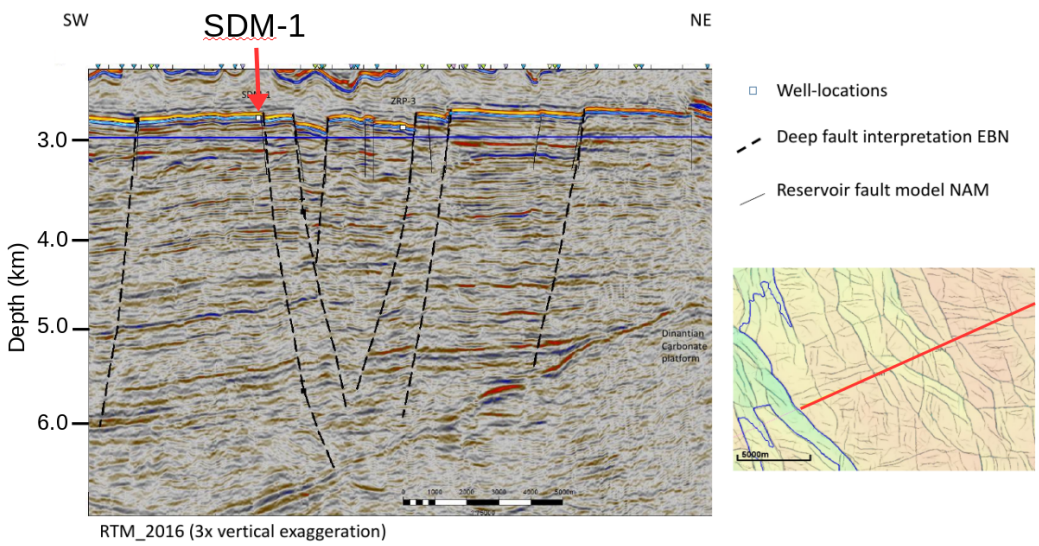

Figure 6.2: A reprocessed seismic section spanning from the Southwest to the Northeast shows a strong reflection at ~6.0 km, and an even deeper one at >7 km dipping to the southwest. (Kortekaas, 2019)(modified)

More recently reprocessed seismic data showed a deeper structure beneath the SDM-01 borehole, as can be seen in figure 6.2 (Kortekaas, 2019). Here a deep formation seems to be dipping towards the Southwest, which would also explain why PS-conversions from South of the borehole should arrive later than those from the North. These observations imply that the discontinuity could also be dipping towards the South.

Our data does not contain events with a back azimuth $0^\circ < \gamma < 90^\circ$ so the subsurface at the North-

east of the borehole could not be estimated with the receiver function method. If we look at events with a back azimuth of $270^\circ < \gamma < 360^\circ$ we do see an earlier PS-arrival for the 6.0 km discontinuity, which indicates that the subsurface should be shallower here, this agrees with van Buggenum and den Hartog Jager (2007), Geluk et al. (2007) and Kortekaas (2019).

7 Conclusion

7.1 General Findings

We have effectively detected multiple PS-conversions by using receiver functions obtained from a vertical array of 3-component geophones. Evidence for multiple discontinuities at depth has been found.

By using 1D elastic modelling, the depth of these discontinuities has been reproduced and it has been inferred that the bottom lower Rotliegend is located at 3.7 km, the bottom Westphalian at 4.7 km, the bottom Namurian at 5.85-6.15 km, and the bottom Dinantian can be found at 6.8 km. These interpretations, while highly tentative, give us a good representation of the 1D structure below the borehole. Due to the lack of an extensive dataset the lateral variations in depth of these discontinuities could not be accurately constrained.

The goal of this research has been to determine the effectiveness of the vertical array receiver function method, and if it can be used to find discontinuities at depth. Based on this research we can say that the vertical array receiver function method is a good method for detecting strong discontinuities. We have shown that the receiver function method, which up until now has only been used on a global scale, is very adequate for finding conversions on a smaller, local scale.

If 3-component geophone data is available, the vertical array receiver function method can be applied on datasets very quickly. This method requires little computation and interpretation time compared to traditional seismics, in which large arrays of geophones have to be deployed, and active sources are required. This method makes use of earthquake sources, which means that besides maintenance of the geophone array, little work is required to obtain the data.

7.2 Further Research

As previously mentioned, the receiver functions that were obtained have shown very convincing proof that the structure below the reservoir differs in different directions, but the coverage was limited. If a more extensive dataset were studied, then a more accurate image of the structure below the reservoir might be obtained.

If we would want to further study the discontinuities near the reservoir without using an entirely new dataset, we might be able to use S-to-P conversion. This method could be performed on the same dataset that PS-conversion has been studied on, making it an attractive option. Since the dataset has already been accurately studied, the S-wave arrival from each event used in this study can be easily determined after which we can again used a water level deconvolution to obtain a converted PS-wave.

There are two major drawbacks with SP conversion. The first drawback is that instead of using the coda of the S-wave which comes **after** the direct S-arrival like we do with PS conversion, we need to take a window before the direct S arrival, known as the S-wave precursor. By processing data that comes before the S-wave arrival, there might be a chance that the SP arrives during the arrival of earlier waves. This could make it very difficult to distinguish the SP-wave. Especially in a setting as this one, where we are looking for small scale discontinuities.

In a future study, instead of using a 1D modelling program, a 3D modelling program might be used to more accurately model the 3D structure below the reservoir. Then tilted layers might also be incorporated, which is more realistic.

All in all, this research has shown that applying the receiver function method on an array of geophones is a very useful method which uses a passive measuring method. If this method were used on more locations the subsurface could be accurately studied.

Acknowledgements

I would like to thank Hanneke Paulssen for her supervision and guidance throughout the the thesis, while the process did undergo some hard times, the input of the supervision never felt too forced and asking questions was encouraged. I also enjoyed the weekly meetings so that each week at least something could be discussed and prevented me from taking too much time on a subject that could have been dealt with quicker.

I would like to thank Ivan Pires the Vasconcelos on supervision of the mathematical aspect on the thesis and advising on the water level deconvolution method.

Another contributor to the work is PhD candidate Wen Zhou, who has also worked with the SDM-01 borehole data and was always open for discussion, and the supply of fresh ideas.

I would like to thank the recently graduated Eva Arwert for providing a lot of the preliminary research on the SDM-01 borehole data, without her work this thesis would not have been possible.

I want to further thank my friends and student colleagues for all of their moral support, discussions, lunches, coffee breaks and other extracurricular activities; Jasper van Weers, Erik van Linden, Sten Jacobs, Tim Bögels, Gijs Munnecom, Dieuwertje Kuijpers, Boris Gesbert, Jort Jansen, Olivier Winkel, Mike Sep, Eldert Fokker, Marius Wouters.

Lastly I would also like to thank my parents, my brother, and my sister for always being there and supporting me whenever necessary.

And a very thanks to my sweet Marloes, you mean the world to me.

References

Aki, K. and Richards, P. G. (2002). *Quantitative seismology*. University Science Books.

Arwert, E. (2019). Determination of lithological interfaces above the Groningen gas field reservoir using RZ-decon of borehole SDM-01 check shot data and synthetics (Msc Thesis). *Utrecht University*.

Brocher, T. M. (2005). Empirical relations between elastic wavespeeds and density in the Earth's crust. *Bulletin of the seismological Society of America*, 95(6):2081–2092.

de Gans, W. (2007). Quaternary. In *Geology of the Netherlands*, pages 151–172. Edita-KNAW.

Geels, M. (2019). Kabinet: gaskraan Groningen acht jaar eerder dicht. https://www.nrc.nl/nieuws/2019/09/10/gaswinning-groningen-al-in-2022-aan-banden-a3972810.

Geluk, M. (2007a). Jurassic. In *Geology of the Netherlands*, pages 107–126. Edita-KNAW.

Geluk, M. (2007b). Permian. In *Geology of the Netherlands*, pages 63–83. Edita-KNAW.

Geluk, M. (2007c). Permian. In *Geology of the Netherlands*, pages 85–106. Edita-KNAW.

Geluk, M., Dusar, M., and De Vos, W. (2007). Pre-Silesian. In *Geology of the Netherlands*, pages 23–38. Edita-KNAW.

Julia, J., Ammon, C. J., Herrmann, R., and Correig, A. M. (2000). Joint inversion of receiver function and surface wave dispersion observations. *Geophysical Journal International*, 143(1):99–112.

Katznelson, Y. (2004). *An introduction to harmonic analysis*. Cambridge University Press.

Kortekaas, M. (2019). Seismic record of the Geology below the SDM-1 borehole. personal communication.

Langston, C. A. (1979). Structure under Mount Rainier, Washington, inferred from teleseismic body waves. *Journal of Geophysical Research: Solid Earth*, 84(B9):4749–4762.

Ligorria, J. P. and Ammon, C. J. (1999). Iterative deconvolution and receiver-function estimation. *Bulletin of the seismological Society of America*, 89(5):1395–1400.

Nábělek, J., Hetényi, G., Vergne, J., Sapkota, S., Kafle, B., Jiang, M., Su, H., Chen, J., Huang, B.-S., et al. (2009). Underplating in the Himalaya-Tibet collision zone revealed by the Hi-CLIMB experiment. *Science*, 325(5946):1371–1374.

Owens, T. J., Zandt, G., and Taylor, S. R. (1984). Seismic evidence for an ancient rift beneath the Cumberland Plateau, Tennessee: A detailed analysis of broadband teleseismic P waveforms. *Journal of Geophysical Research: Solid Earth*, 89(B9):7783–7795.

Rondenay, S. (2009). Upper mantle imaging with array recordings of converted and scattered teleseismic waves. *Surveys in geophysics*, 30(4-5):377–405.

Stein, S. and Wysession, M. (2009). *An introduction to seismology, earthquakes, and earth structure*. John Wiley & Sons.

TNO (2019). DINO-loket. https://www.nlog.nl/kaart-boringen.

van Buggenum, J. M. and den Hartog Jager, D. G. (2007). Silesian. In *Geology of the Netherlands*, pages 43–62. Edita-KNAW.

van Weers, J. (2019). Hypocenter Relocation in Groningen using the Double-Difference Method (Msc thesis). *Utrecht University*.

Wapenaar, K. (2019). elastic1d (personal communiation).

Whaley, J. (2009). The Groningen Gas Field. *Geo Expro*, 6.

Wong, T. (2007). Cretaceous. In *Geology of the Netherlands*, pages 127–150. Edita-KNAW.

Wong, T., Batjes, D., and de Jager, J. (2007a). *Geology of the Netherlands*. Edita-KNAW.

Wong, T. E., de Lugt, I. R., Kuhlmann, G., and Overeem, I. (2007b). Tertiary. In *Geology of the Netherlands*, pages 151–172. Edita-KNAW.

Xu, L., Rondenay, S., and van der Hilst, R. D. (2007). Structure of the crust beneath the southeastern Tibetan Plateau from teleseismic receiver functions. *Physics of the earth and planetary interiors*, 165(3-4):176–193.

Zhou, W. and Paulssen, H. (2017). P and S velocity structure in the Groningen gas reservoir from noise interferometry. *Geophysical Research Letters*, 44(23):11–785.

A Events occurring during the time of deployment

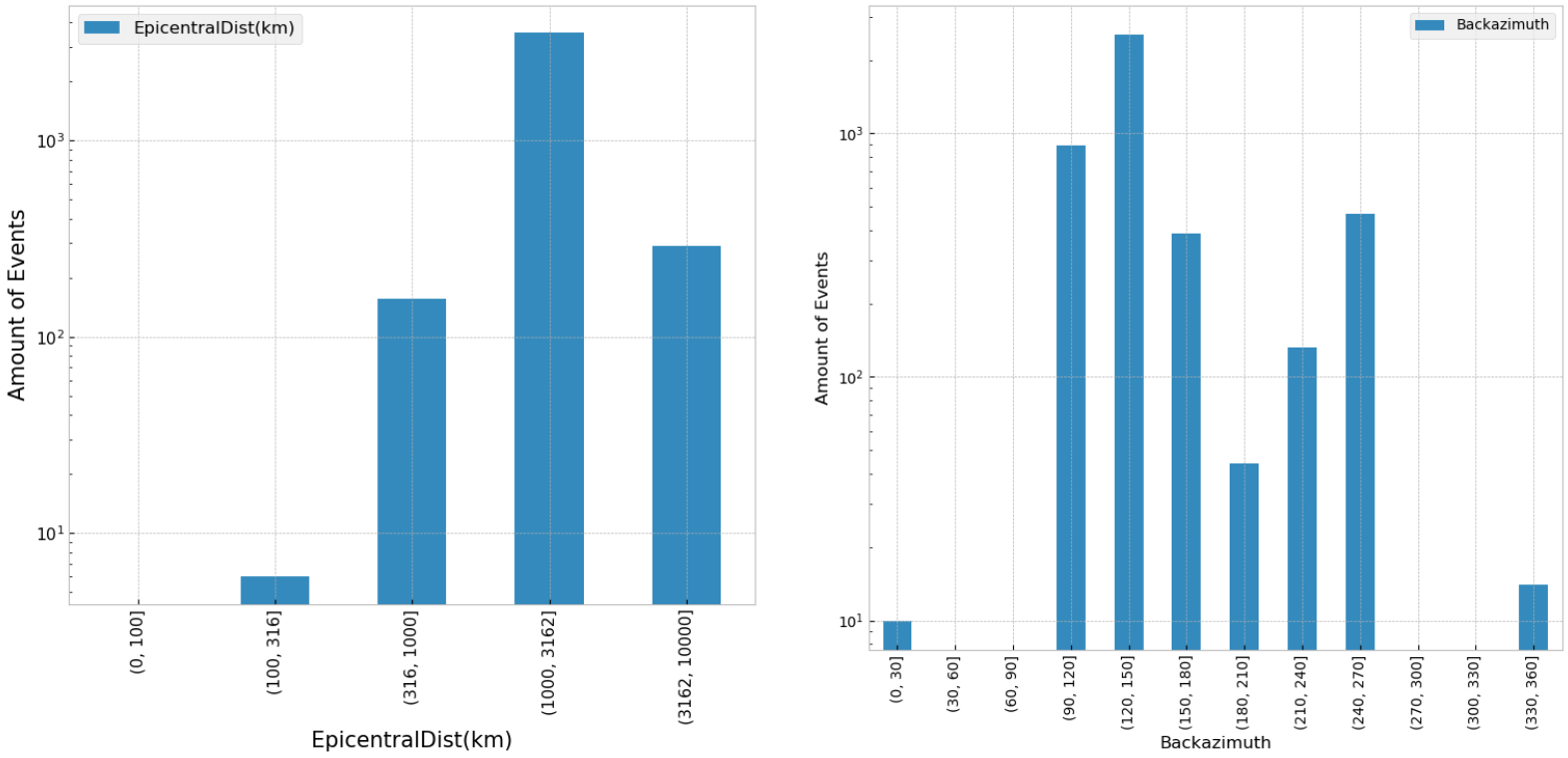

Figure A.1: (left) The amount of events sorted by distance. Note that there is a very small amount of events close to the SDM-01 borehole. (right) The amount of events sorted by back azimuth. It becomesc clear that a large amount of events originate in the West and that events from the West and from the North-East are absent, which means there is no data coverage from these directions.

B Displacement of Transmitted and Converted Waves

In this section, we describe the qualities of reflection and transmission coefficients following Aki and Richards. Note that while in Aki and Richards Z is positively downward, in the data from the SDM-01 geophones the positive Z direction is upward.

When an upgoing P wave crosses an interface with a velocity increase, the upward transmission coefficient $\acute{P}\acute{P} < 1$, and the reflection coefficient $\acute{P}\grave{P} > 0$.

For an upgoing P wave both the vertical component the radial component are both either measured as positive or both are measured as negative. When a P wave is reflected, the sign of the displacement of the radial component is always opposite to that of the vertical component, this can be seen in figure B.1.

For an S-wave the opposite holds, when an upgoing S wave with positive displacement along the Z axis has a negative displacement along the Radial axis. A downgoing S wave always has the displacement on both axes as either positive or negative.

A complete drawing describing the displacement of different transmitted and reflected waves can be seen in figure B.1.

Using these relations and the values for displacement we have converted the pure P-wave and S-wave data to vertical and radial components as follows

$$\begin{aligned} Z_{synthetic} = \cos(i_2)\acute{P}\acute{P} + \sin(j_2)\acute{P}\acute{S} + \\ \sin(j_2)\acute{S}\acute{S} + \cos(i_2)\acute{S}\acute{P} + \\ \sin(i_1)\grave{P}\grave{P} + \cos(j_1)\grave{P}\grave{S} + \\ \cos(j_1)\grave{S}\grave{S} + \sin(i_1)\grave{S}\grave{P} \end{aligned} \tag{B.1}$$

$$\begin{aligned} R_{synthetic} = \sin(i_2)\acute{P}\acute{P} - \cos(j_2)\acute{P}\acute{S} - \\ \cos(j_2)\acute{S}\acute{S} + \sin(i_2)\acute{S}\acute{P} - \\ \cos(i_1)\grave{P}\grave{P} - \sin(j_1)\grave{P}\grave{S} - \\ \cos(j_1)\grave{S}\grave{S} - \sin(i_1)\grave{S}\grave{P} \end{aligned} \tag{B.2}$$

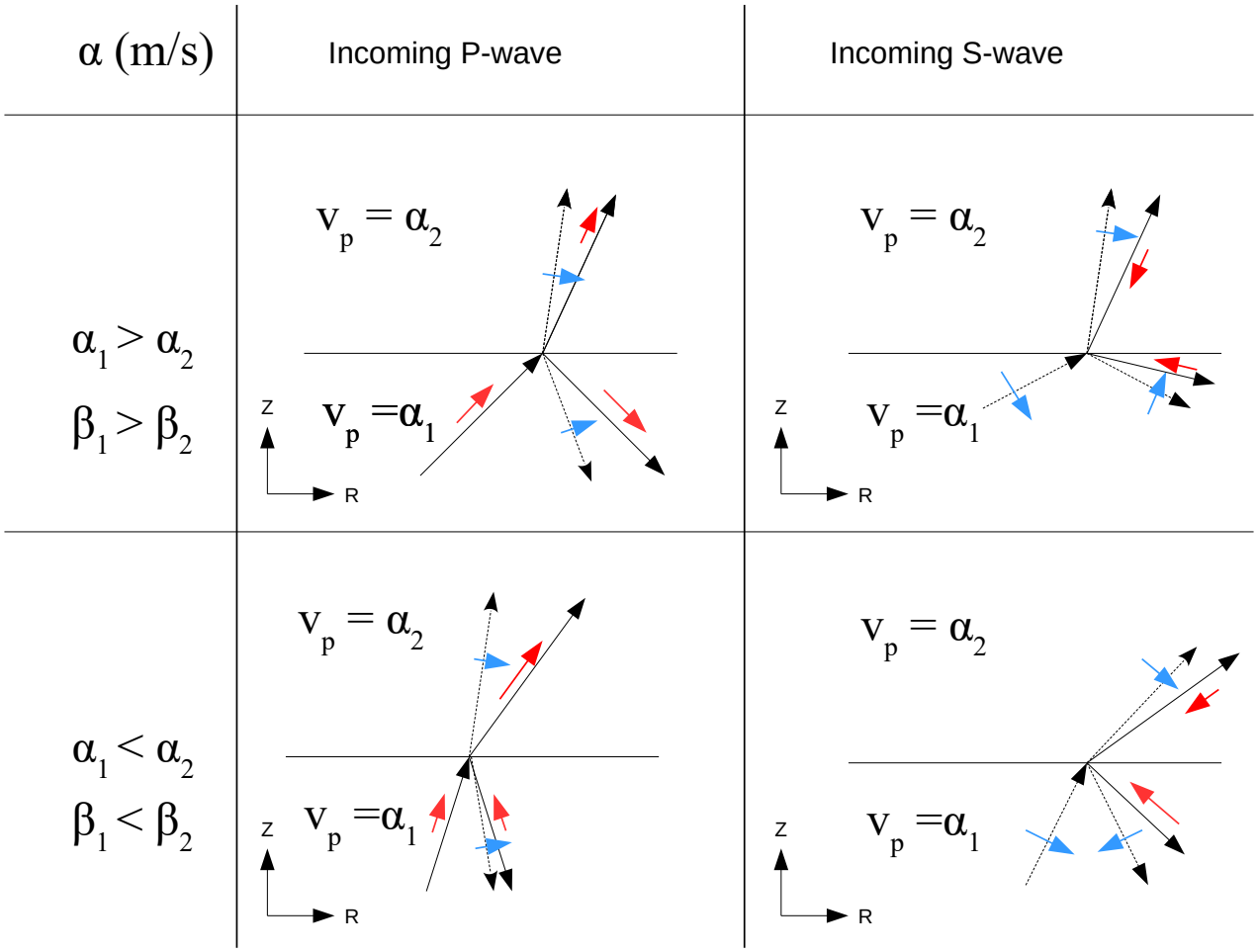

Figure B.1: Displacement directions after a discontinuity, black unbroken lines and red lines denote P wave propagation and particle motion respectively, while dotted lines and blue lines denote S-wave propagation direction and particle motion

C All Receiver Functions

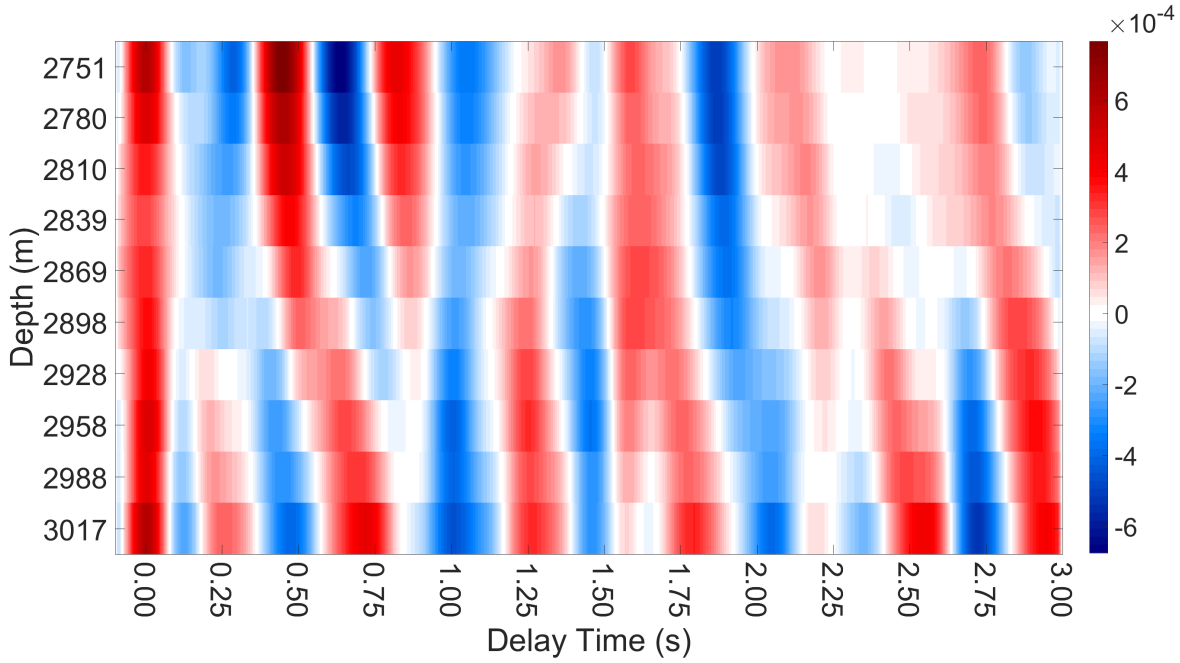

Figure C.1: GREECE-338758-3 Seconds

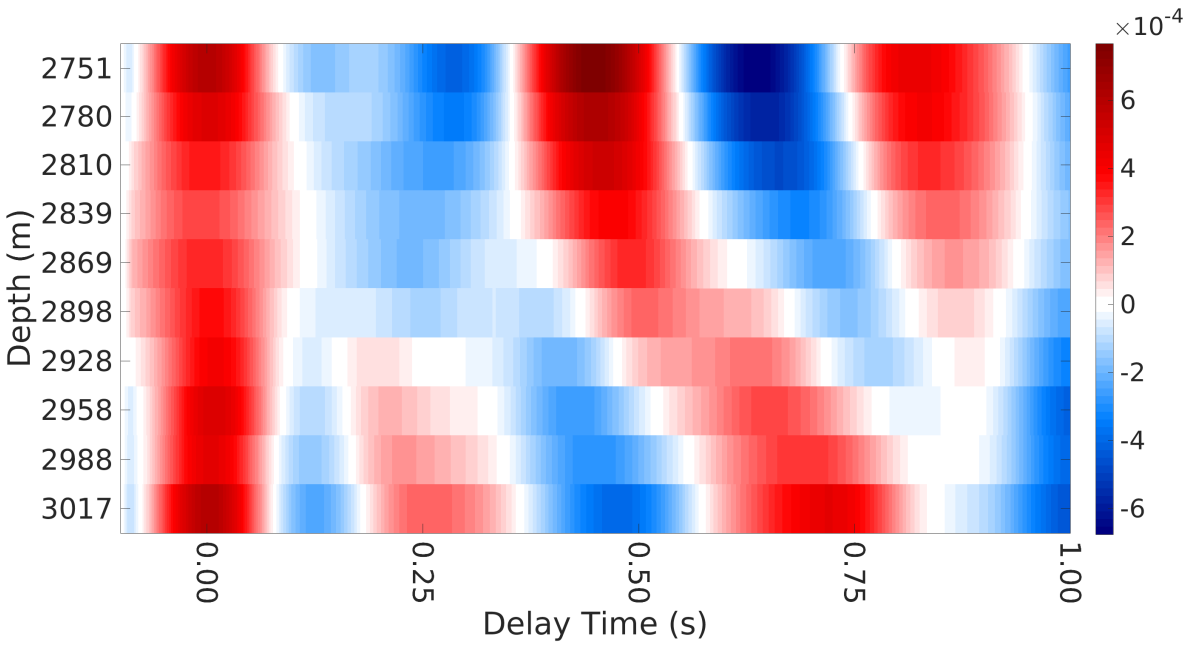

Figure C.2: GREECE-338758-1 Second

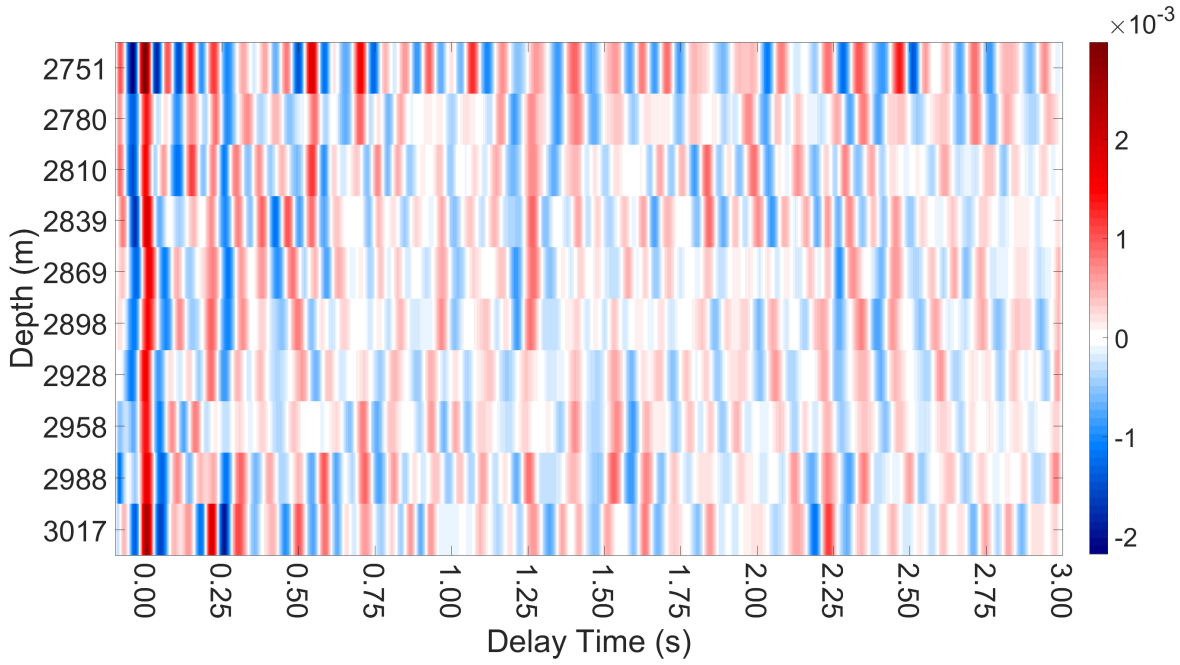

Figure C.3: FRANCE-347777-3 Seconds

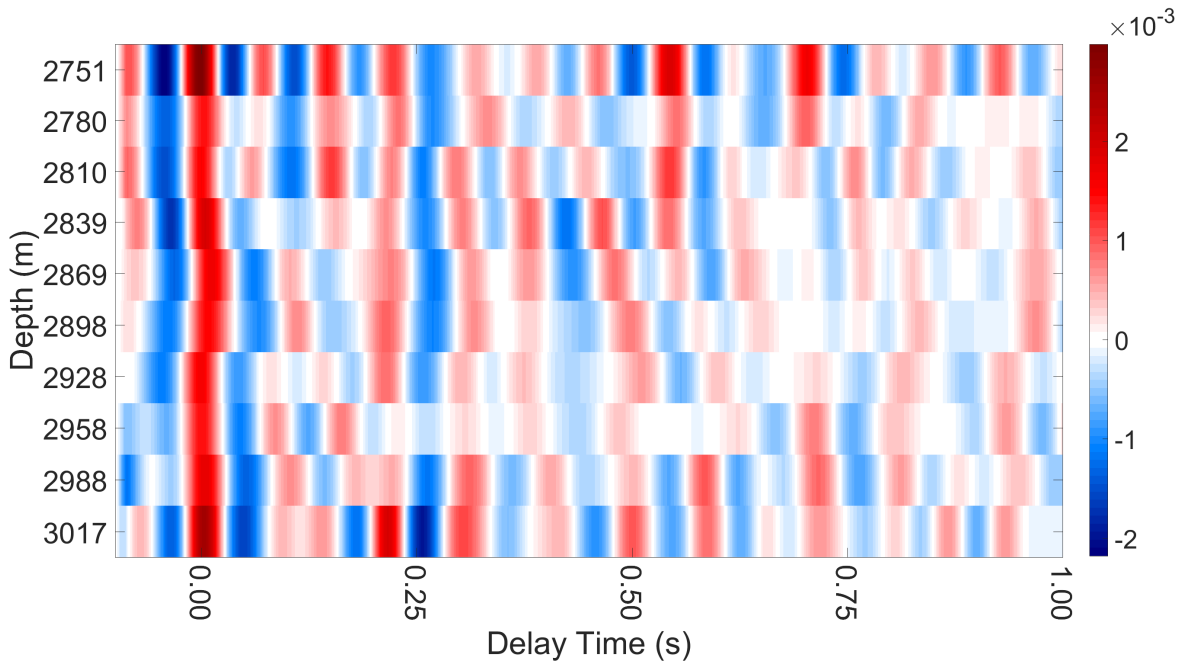

Figure C.4: FRANCE-347777-1 Second

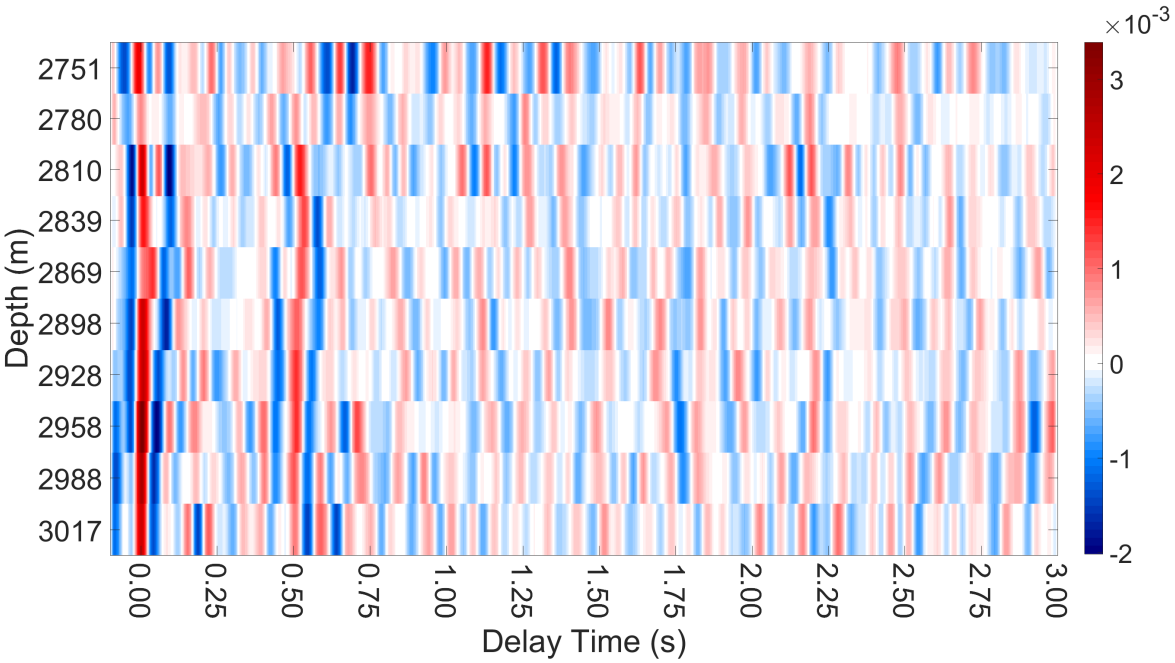

Figure C.5: FRANCE-344701-3s Seconds

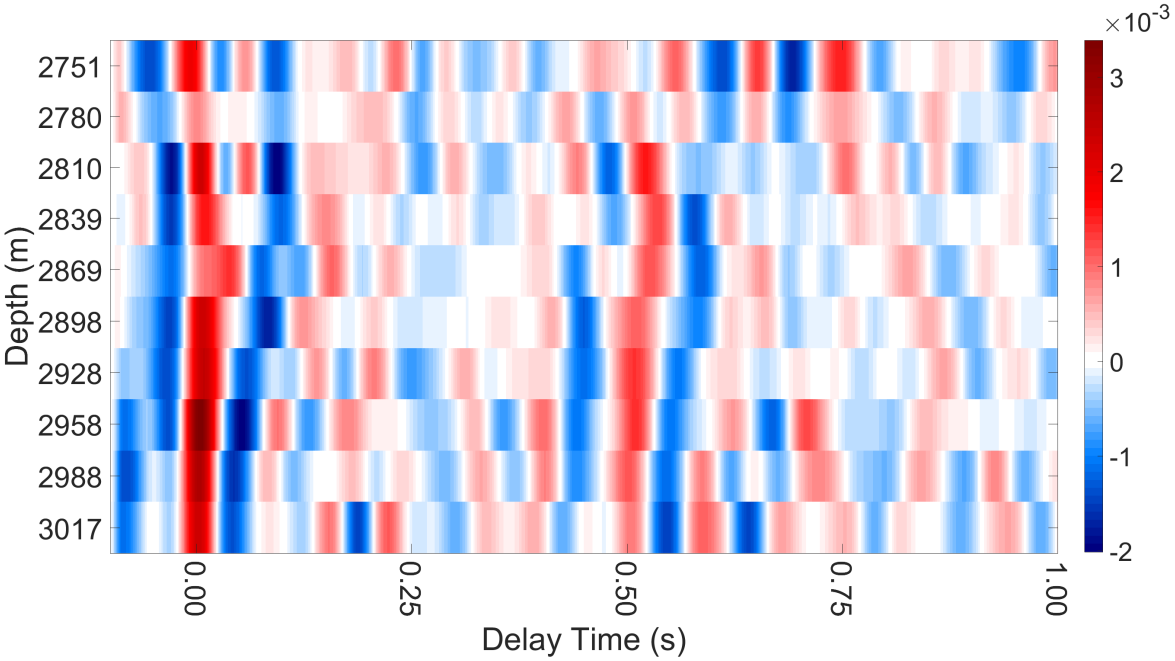

Figure C.6: FRANCE-344701-1 Second

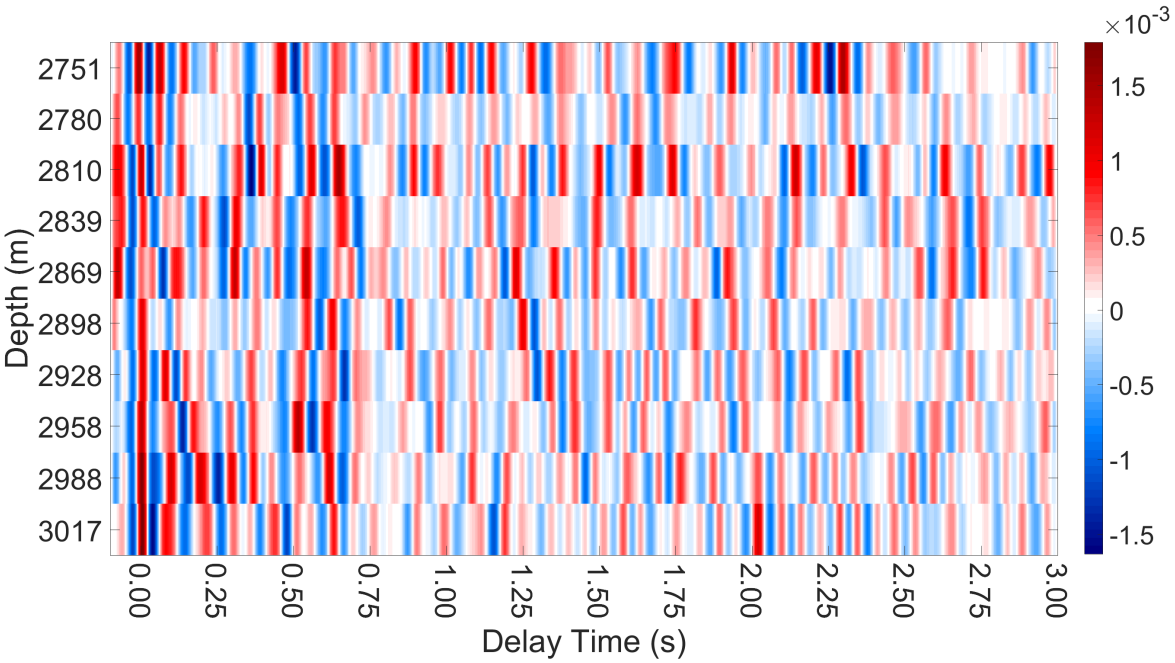

Figure C.7: GERMANY-346178-3 Seconds

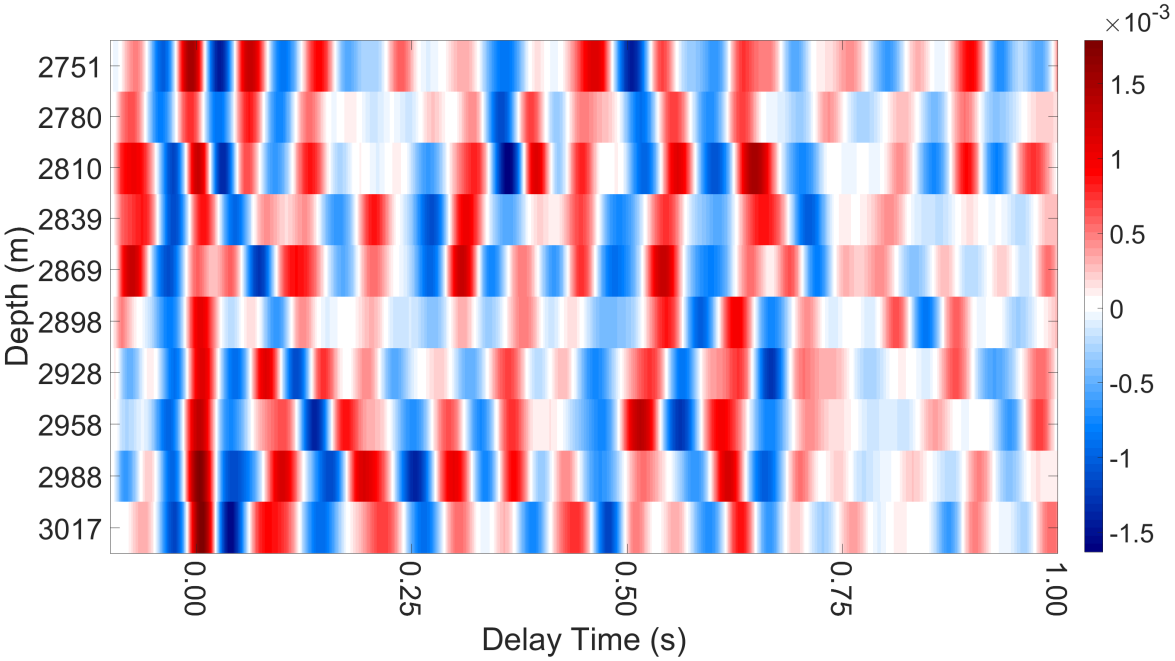

Figure C.8: GERMANY-346178-1 Second

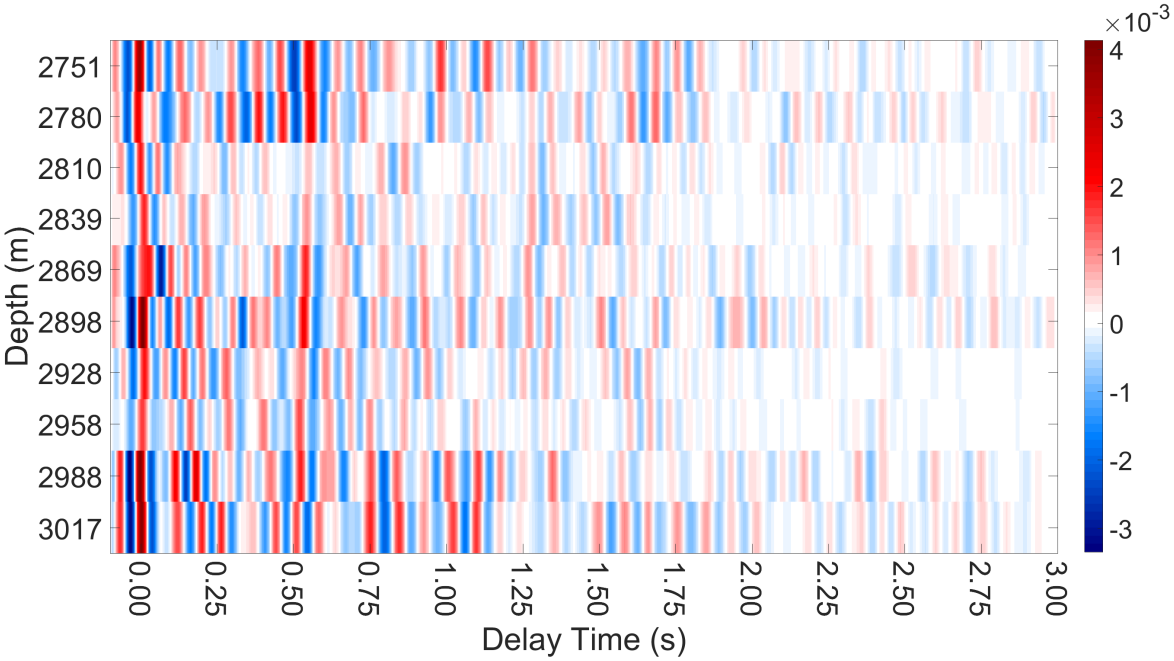

Figure C.9: GERMANY-346847-3 Seconds

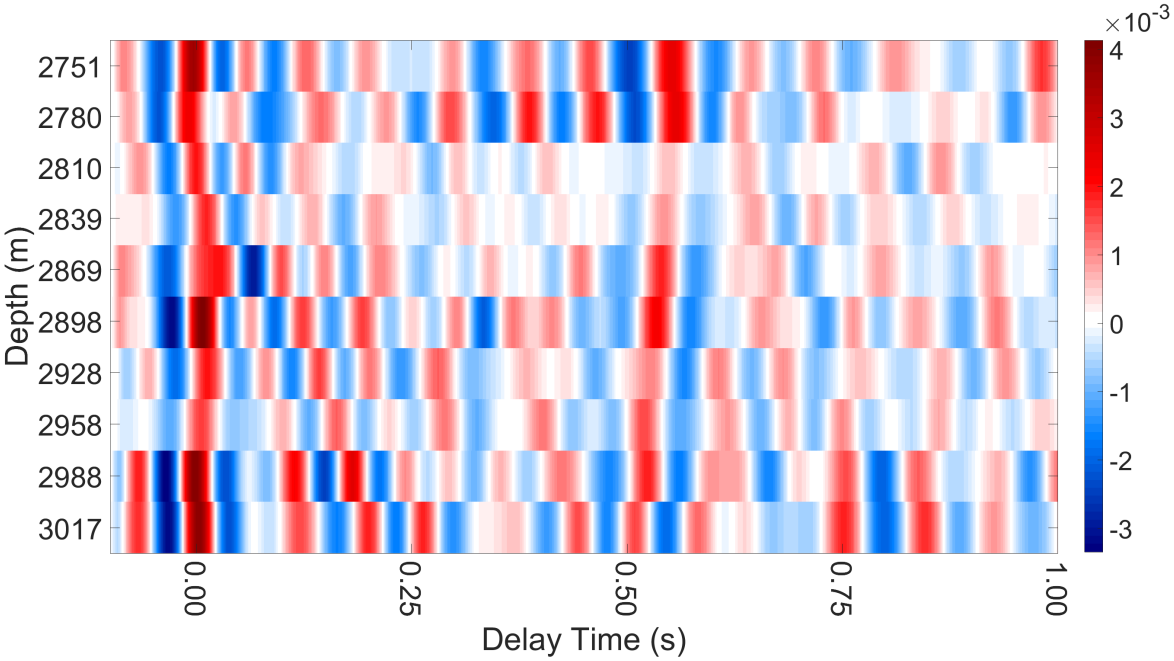

Figure C.10: GERMANY-346847-1 Second

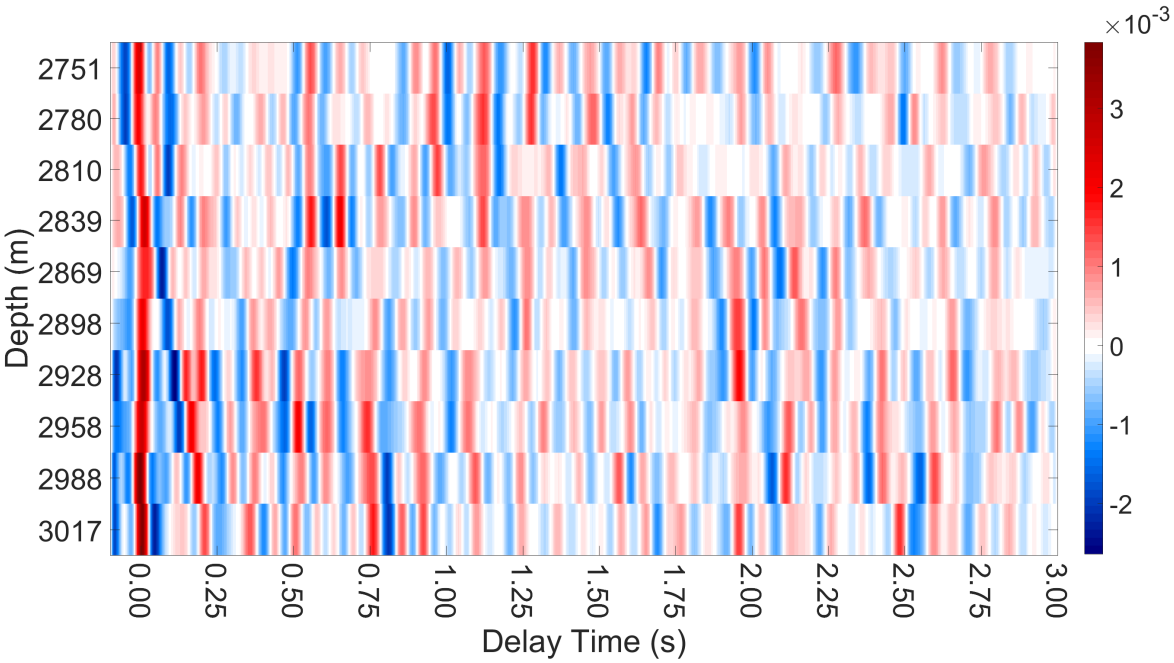

Figure C.11: GERMANY-348421-3 Seconds

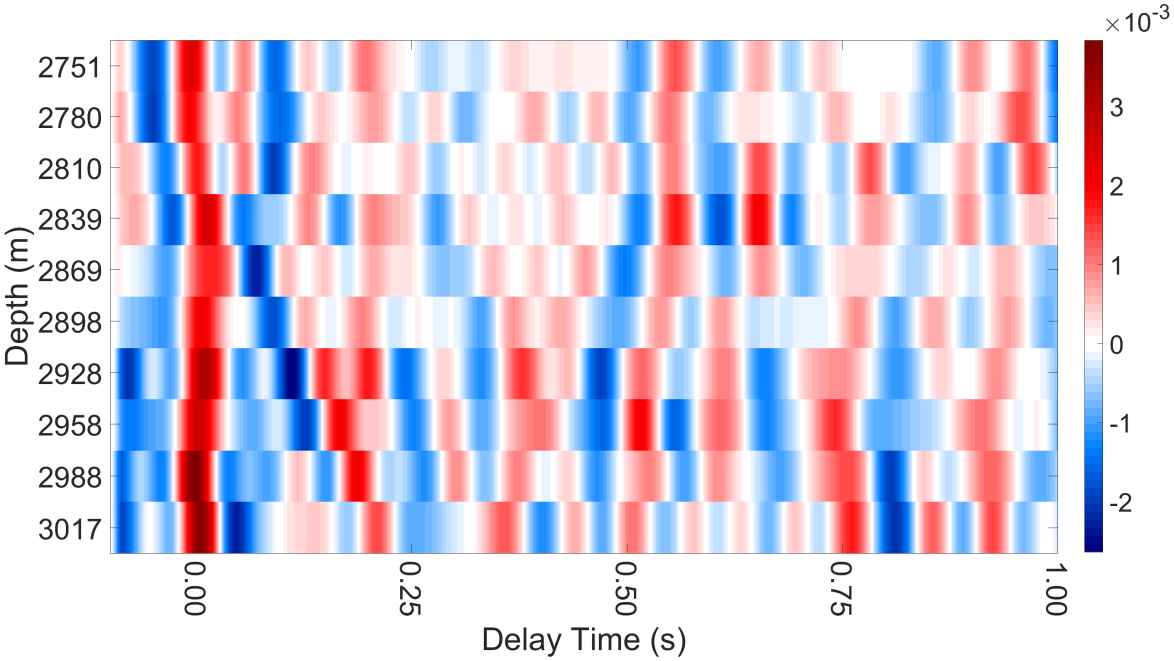

Figure C.12: GERMANY-348421-1 Second

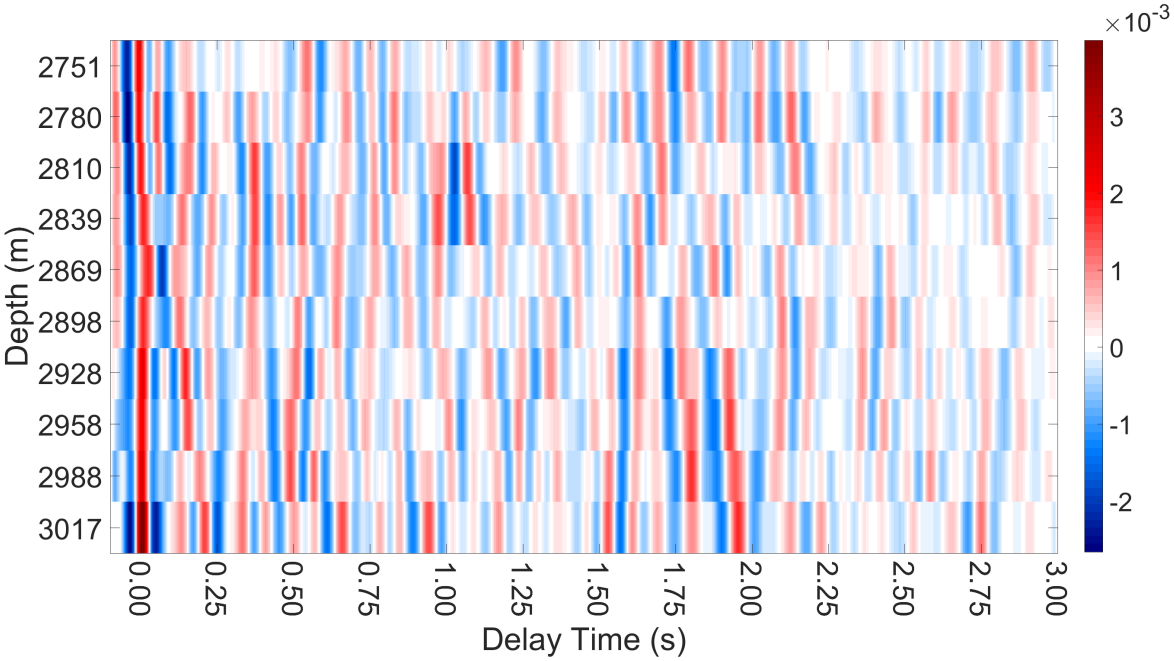

Figure C.13: GERMANY-349422-3 Seconds

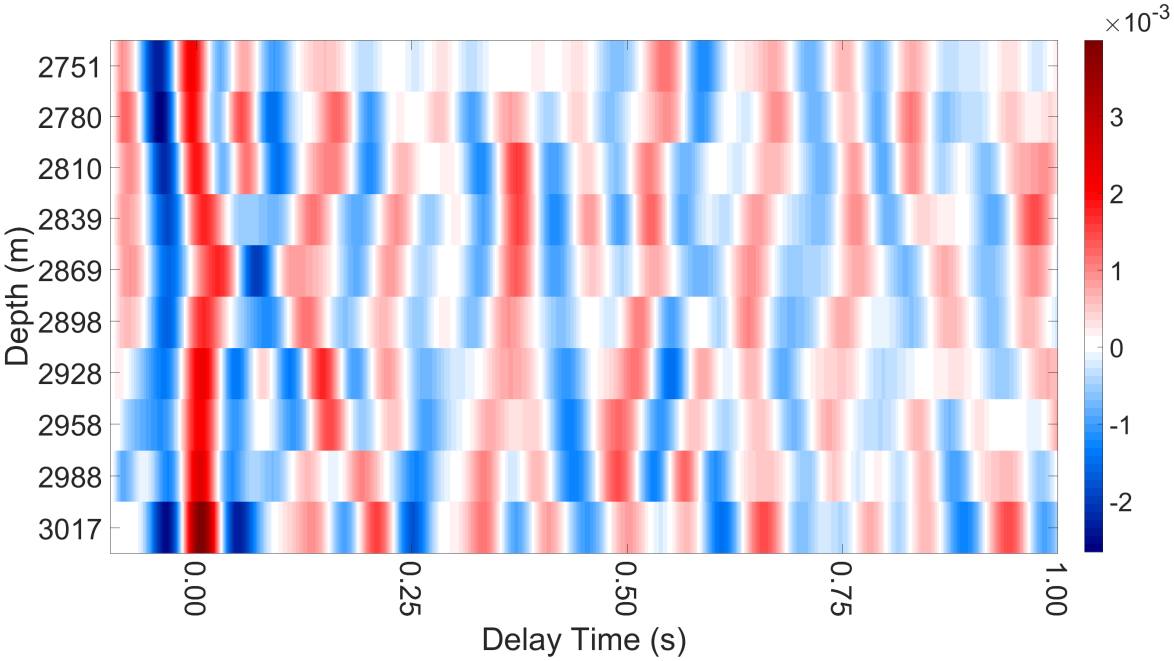

Figure C.14: GERMANY-349422-1 Second

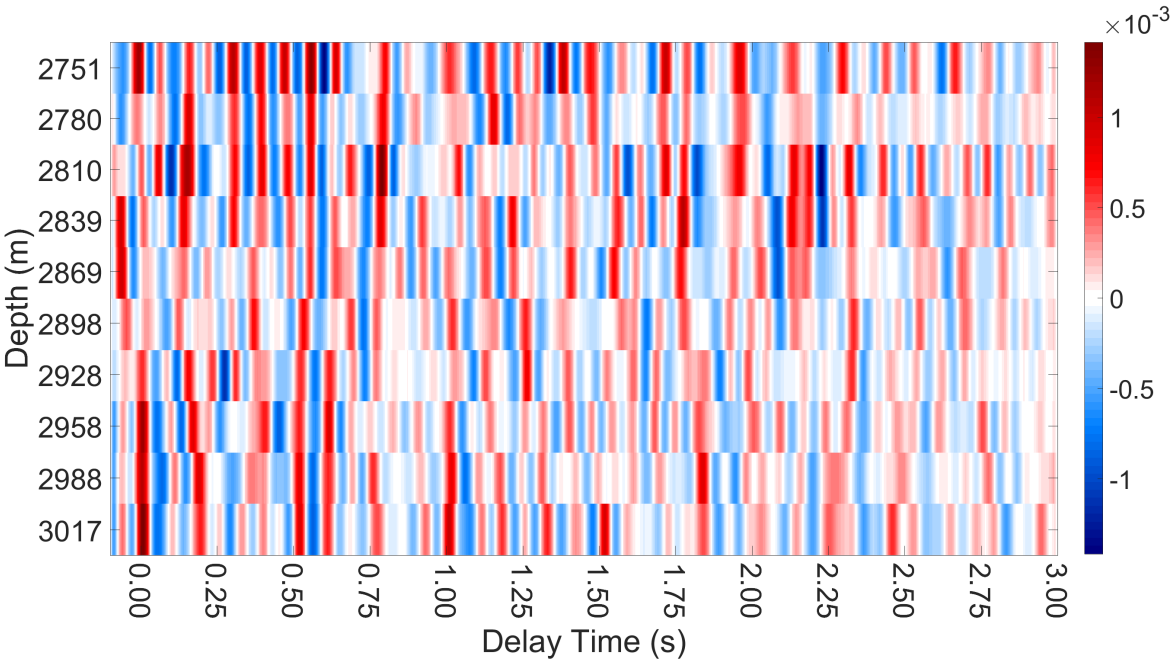

Figure C.15: LIECHTENSTEIN-347750-3 Seconds

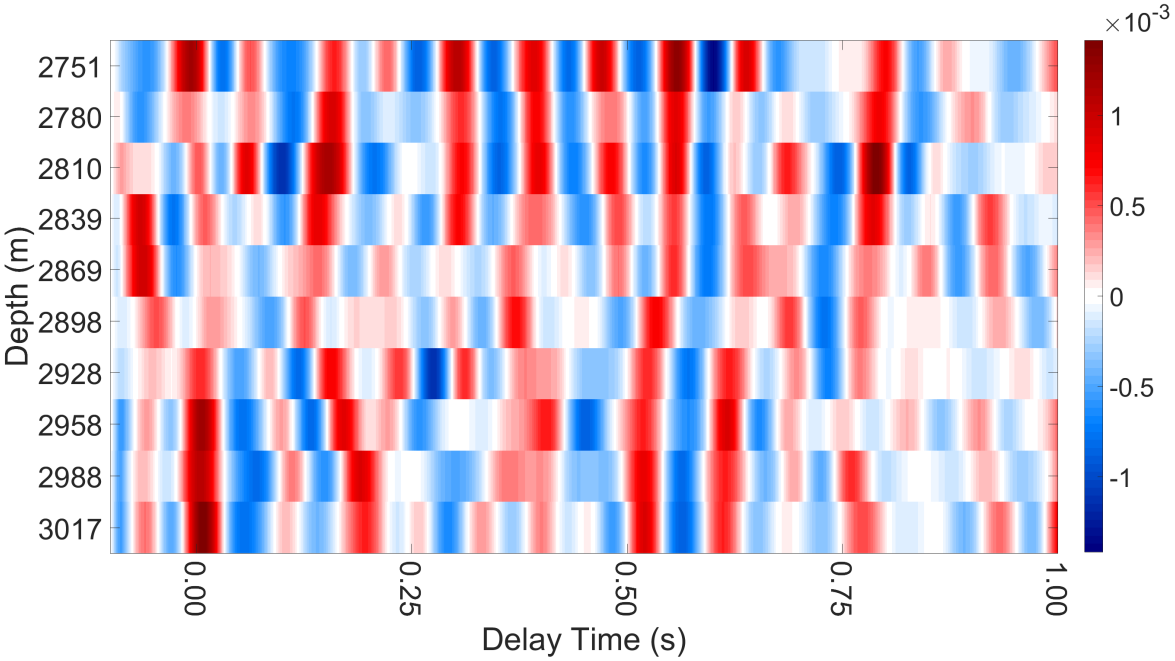

Figure C.16: LIECHTENSTEIN-347750-1 Second

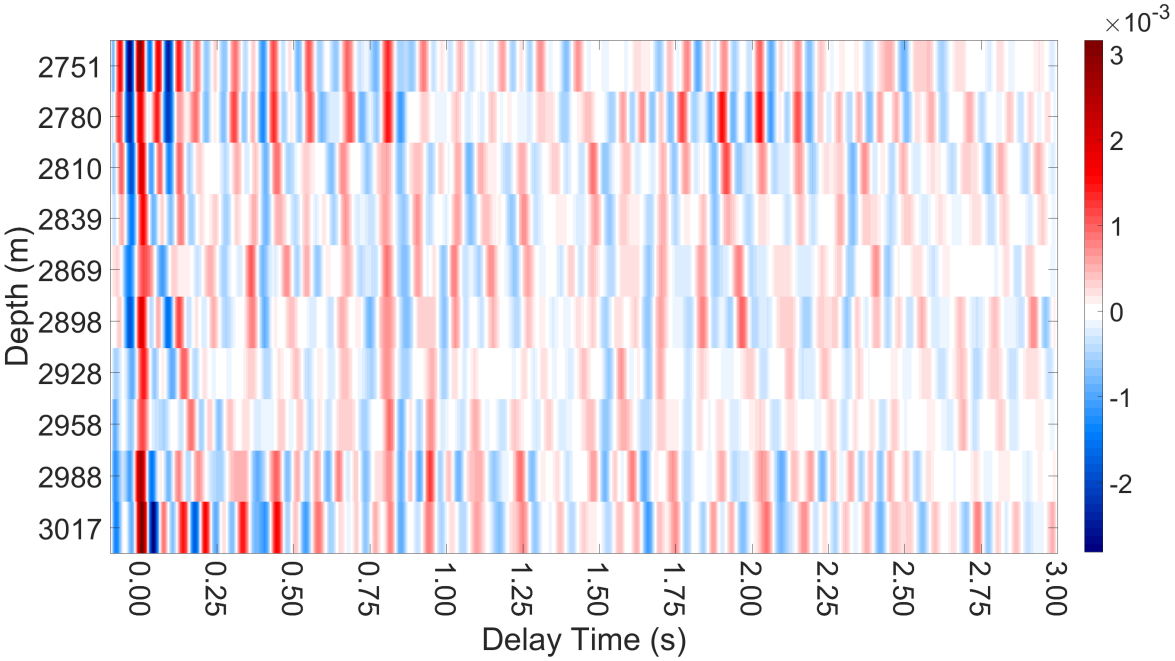

Figure C.17: NORTHSEA-340633-3 Seconds

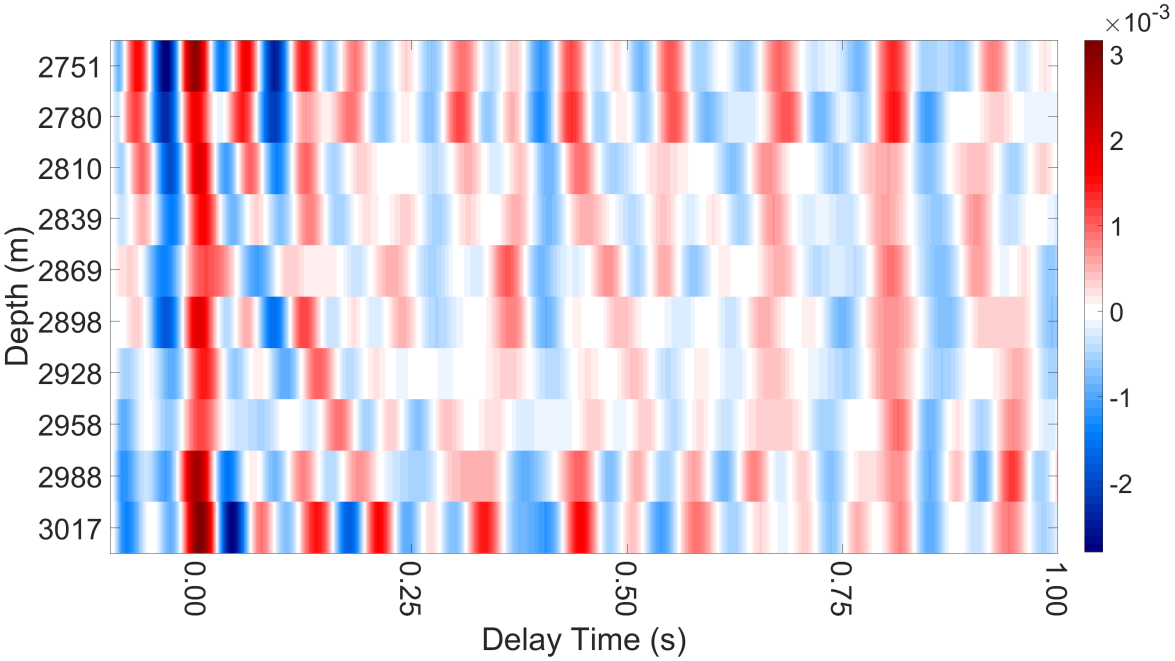

Figure C.18: NORTHSEA-340633-1 Second

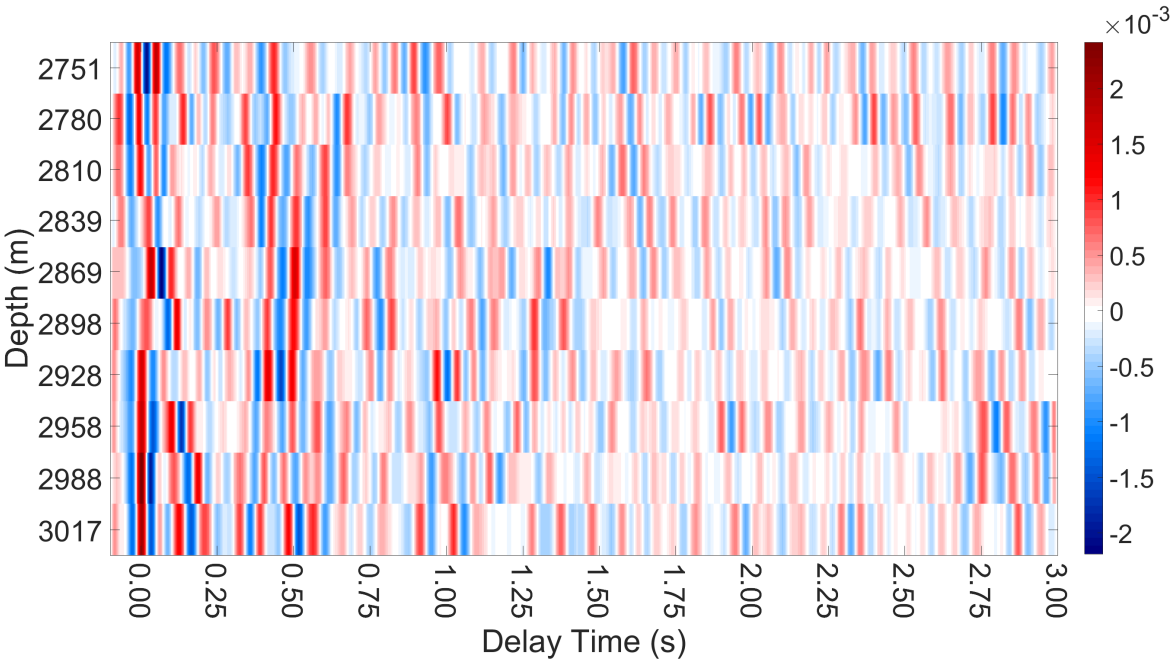

Figure C.19: NORTHSEA-341250-3 Seconds

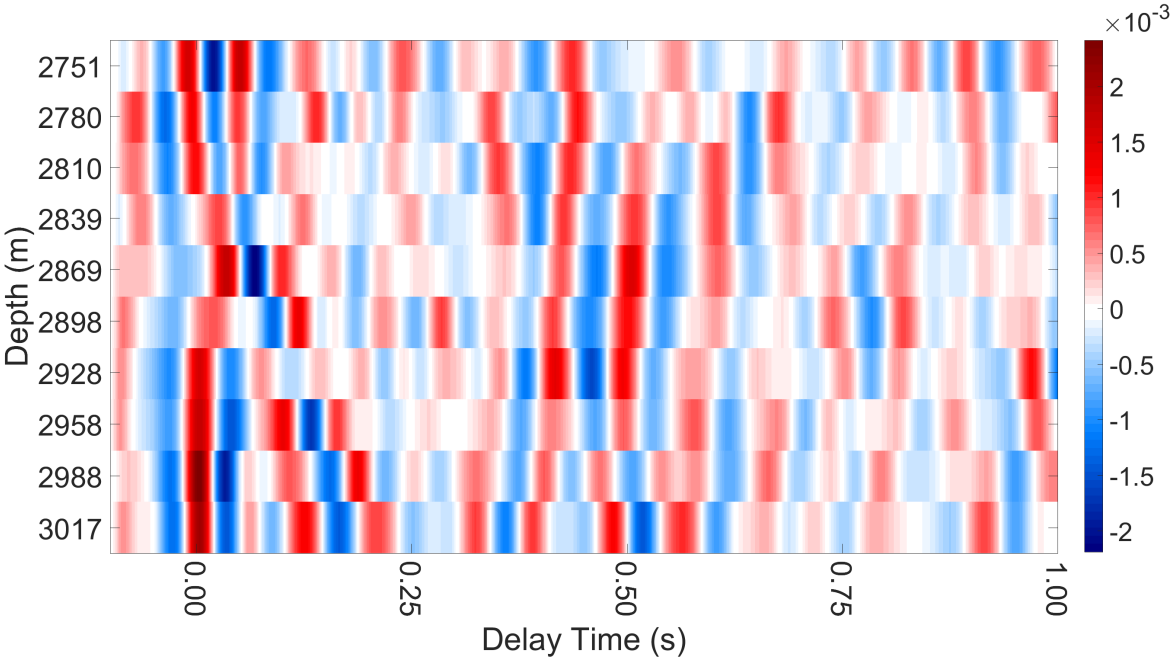

Figure C.20: NORTHSEA-341250-1 Second

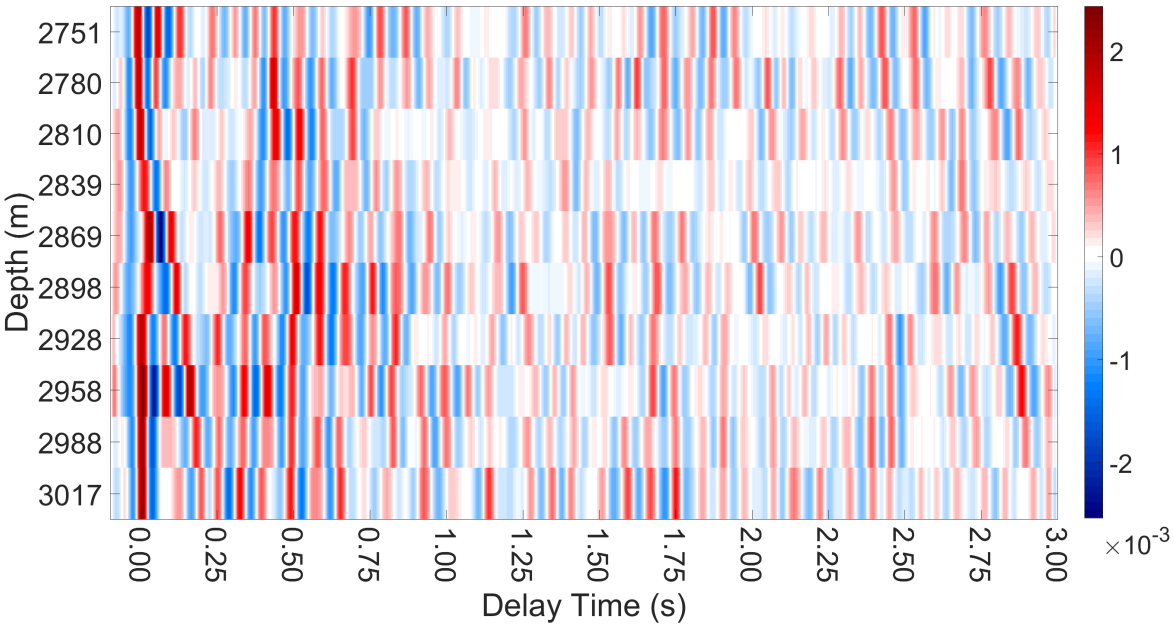

Figure C.21: NORTHSEA-3463993 3 Seconds

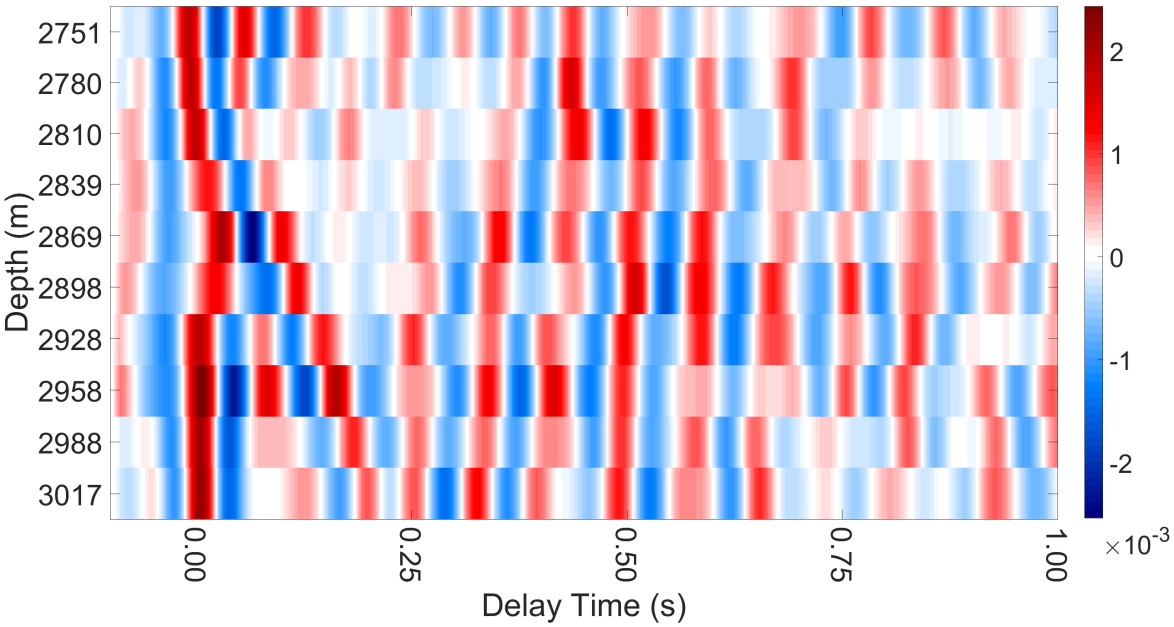

Figure C.22: NORTHSEA-3463993-1 second

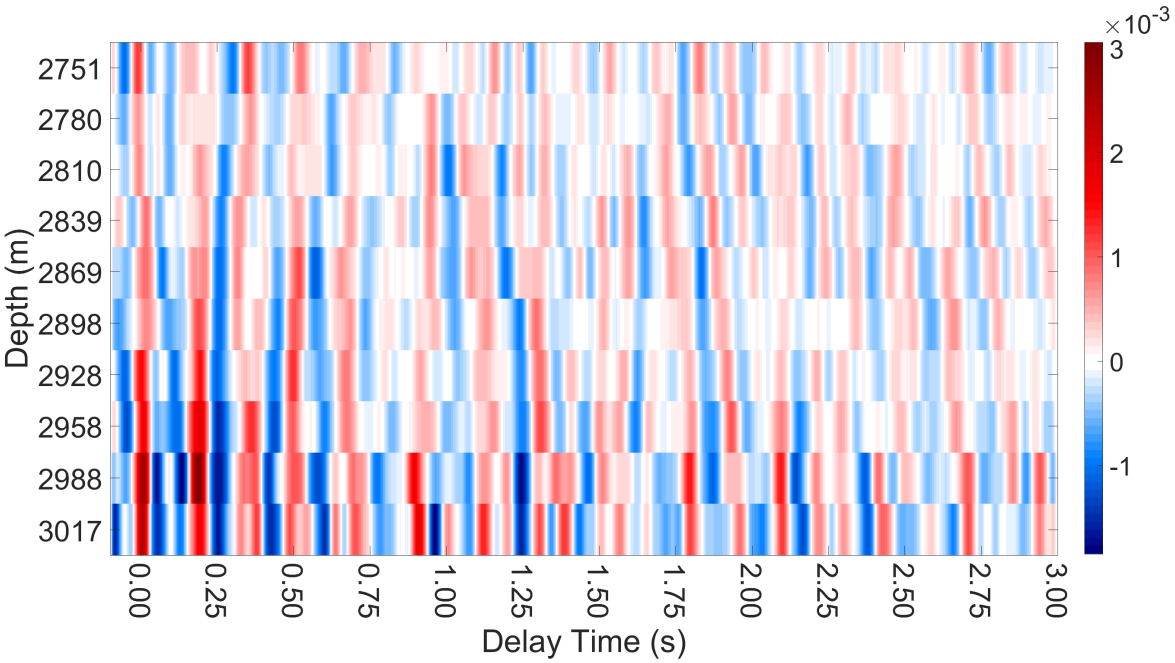

Figure C.23: POLAND-343650-3 Seconds

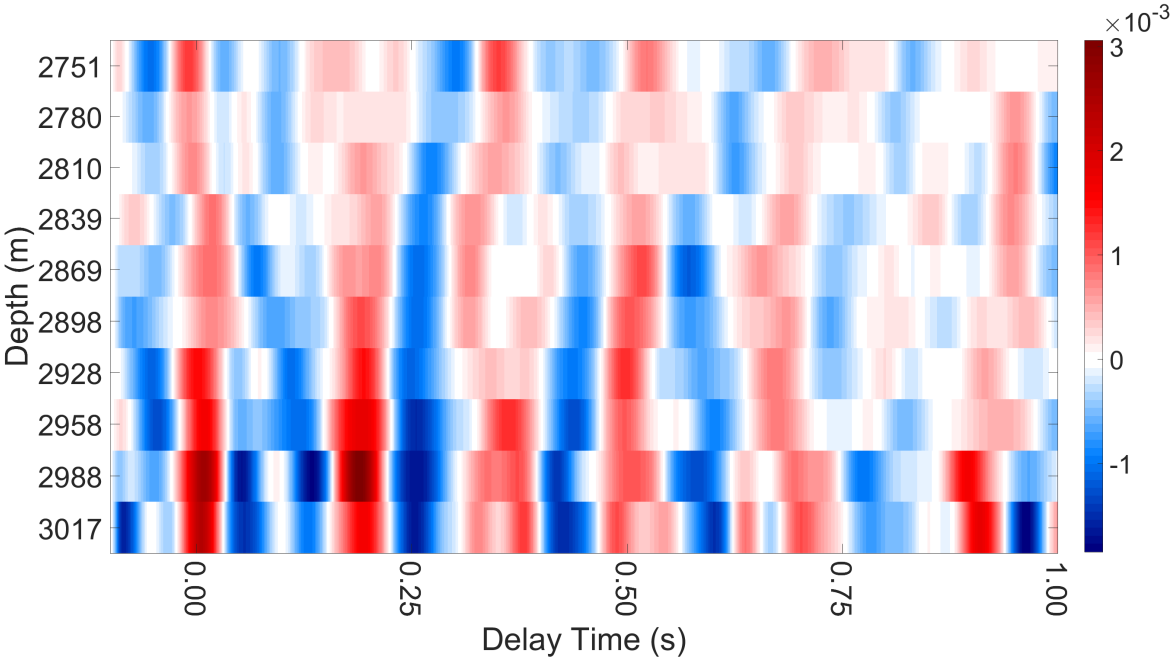

Figure C.24: POLAND-343650-1 Second

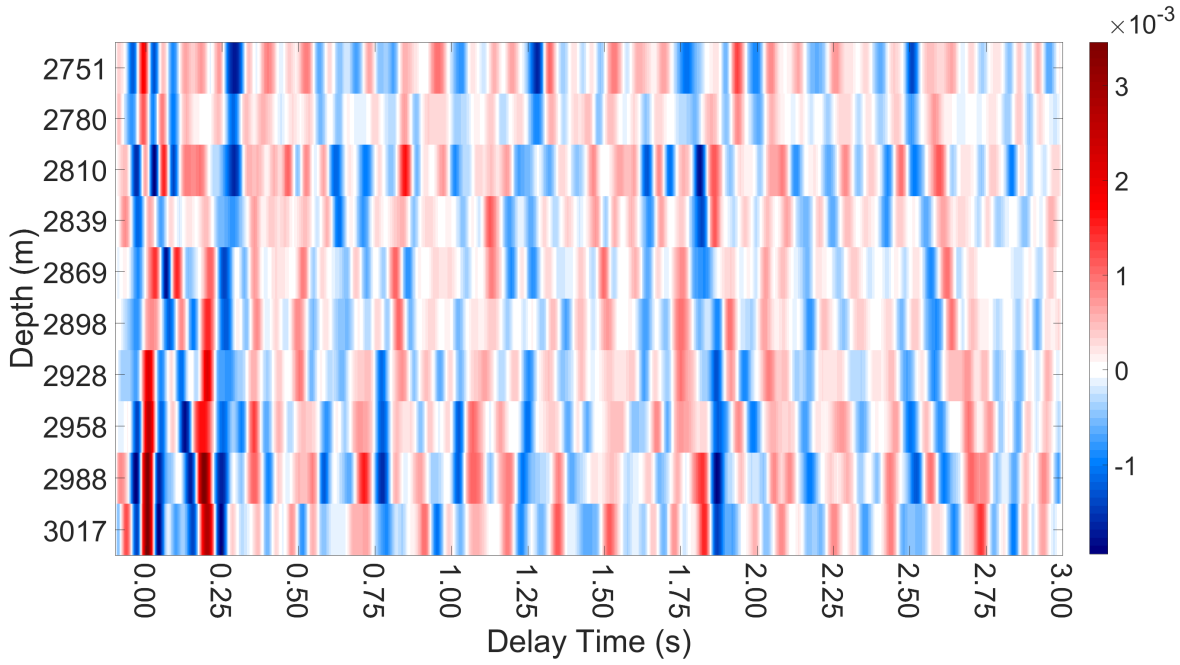

Figure C.25: POLAND-345140-3 Seconds

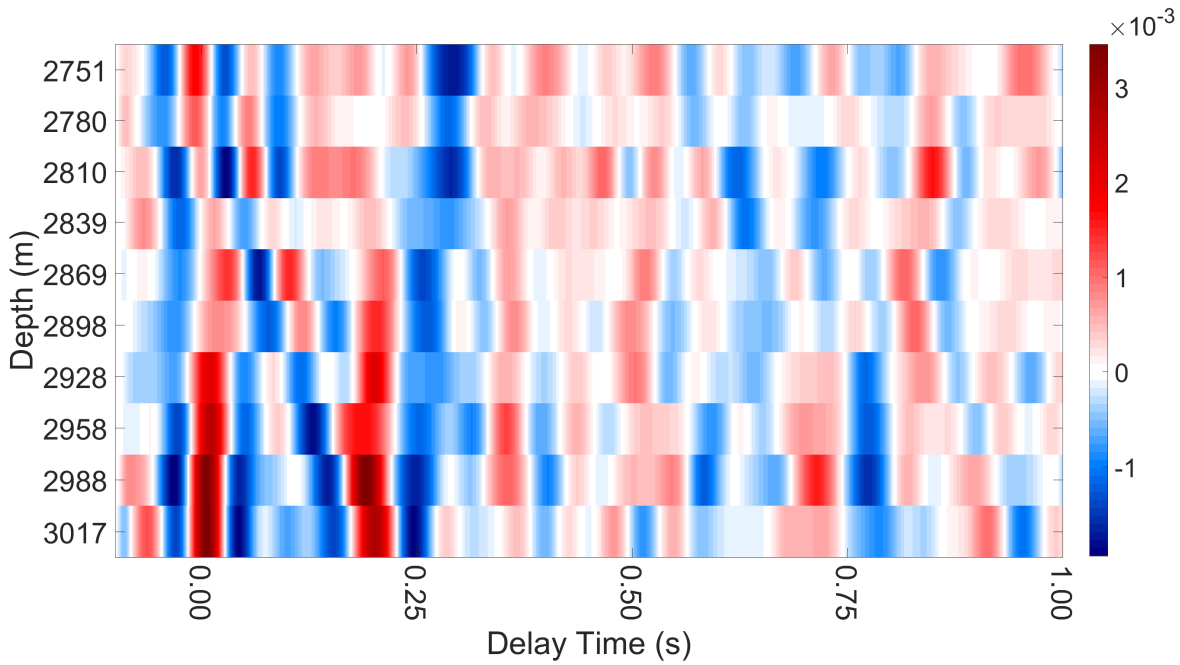

Figure C.26: POLAND-345140-1 Second

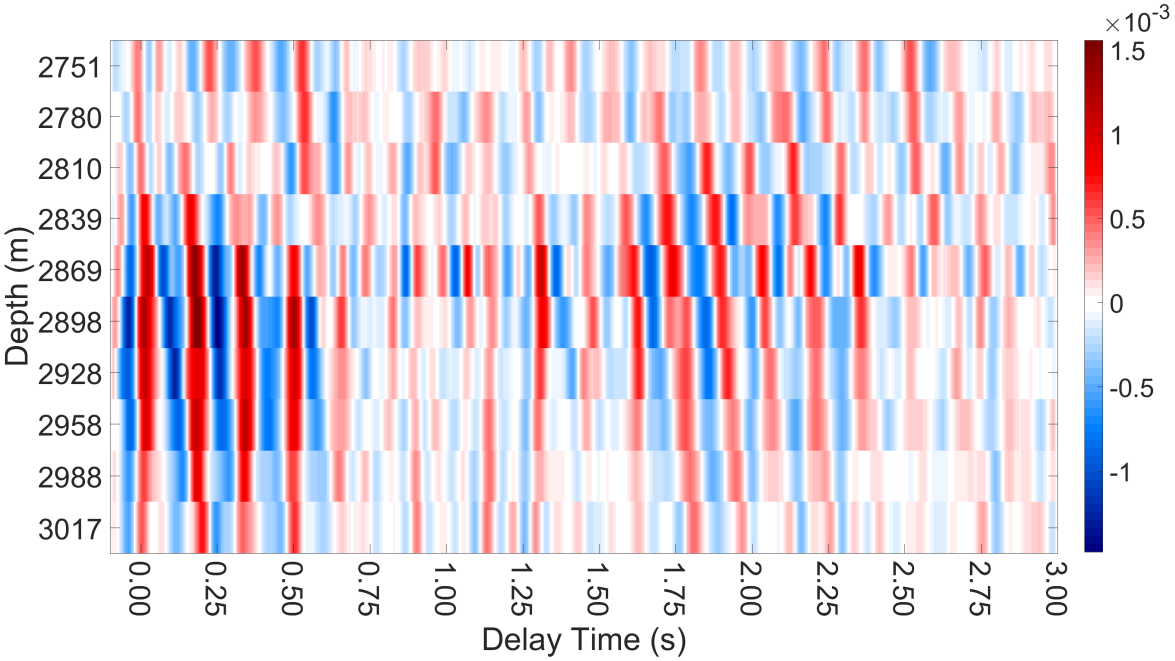

Figure C.27: POLAND-347501-3 Seconds

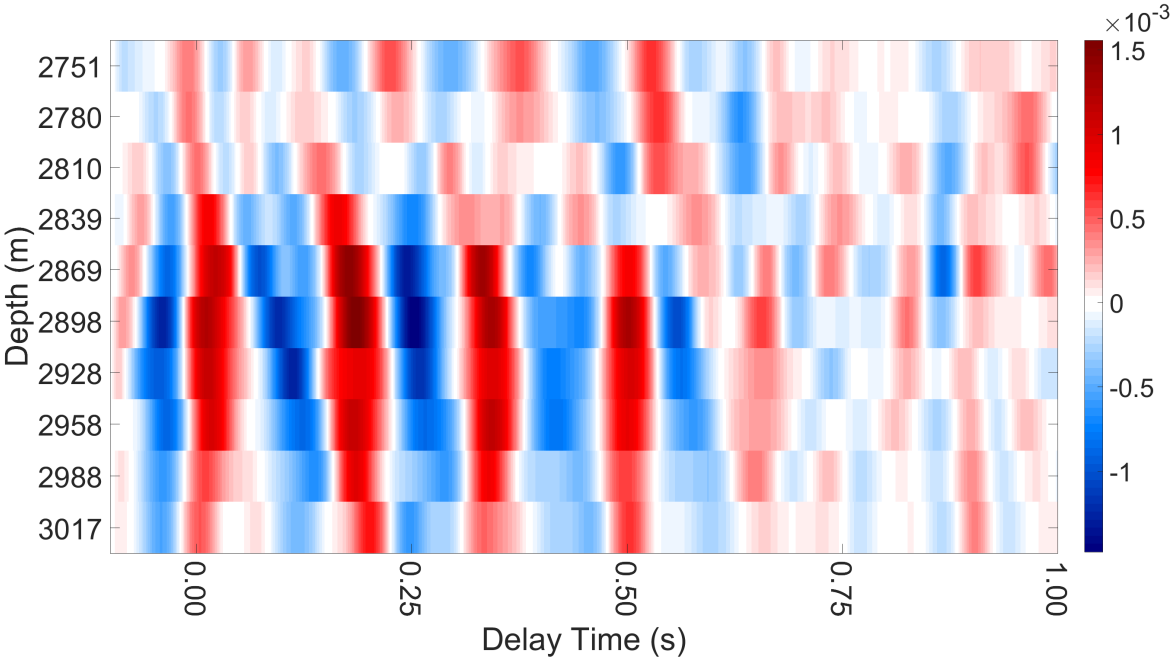

Figure C.28: POLAND-347501- 1 Second